

Contrasting seasonal isotopic signatures of near-surface atmospheric water vapour in the Central Arctic during the MOSAiC campaign

Camilla Francesca Brunello¹, H Meyer¹, M Mellat¹, M Casado¹, S Bucci¹, M Dütsch¹, and M Werner¹

¹Affiliation not available

March 25, 2024

Abstract

The Arctic is experiencing unprecedented moistening, which is expected to have far-reaching impact on global climate and weather patterns. However, it remains unclear whether this newly-sourced moisture originates locally from ice-free ocean regions or is advected from lower latitudes. In this study, we use water vapour isotope measurements in combination with trajectory-based diagnostics and an isotope-enabled AGCM, to assess seasonal shifts in moisture sources and transport pathways in the Arctic. Continuous measurements of near-surface vapour, $\delta^{18}\text{O}$, and δD were performed onboard RV Polarstern during the MOSAiC expedition from October 2019 to September 2020. Combining this isotope dataset with meteorological observations reveals that the spatiotemporal evolution of $\delta^{18}\text{O}$ mimics changes in local temperature and humidity at synoptic to seasonal time scales, while corresponding d-excess changes suggest a seasonal shift in the origin of moisture. Simulation results from the particle dispersion model FLEXPART support these findings, indicating that summer moisture originates from nearby open ocean, while winter moisture comes from more remote sources with longer residence time over sea-ice. Results from a nudged ECHAM6-wiso simulation also indicate that evaporative processes from the ocean surface reproduce summer isotope values, but are insufficient to explain measured winter isotope values. Our study provides the first isotopic characterization of Central Arctic moisture over the course of an entire year, helping to differentiate the influence of local processes versus large-scale vapour transport on Arctic moistening. Future process-based investigations should focus on assessing the non-equilibrium isotopic fractionation during air mass transformation over sea-ice.

1 **Contrasting seasonal isotopic signatures of near-surface atmospheric** 2 **water vapour in the Central Arctic during the MOSAiC campaign**

3 C.F. Brunello ^[1], H. Meyer ^[2], M. Mellat ^[2], M. Casado ^[3], S. Bucci ^[4], M. Dütsch ^[4], M. Werner ^[1]

4 [1] Alfred Wegener Institute, Helmholtz Centre for Polar and Marine Research, Bremerhaven, Germany

5 [2] Alfred Wegener Institute, Helmholtz Centre for Polar and Marine Research, Potsdam, Germany

6 [3] Laboratoire des Sciences du Climat et de l'Environnement, CEA–CNRS–UVSQ–Paris-Saclay–IPSL, Gif-sur-
7 Yvette, France

8 [4] Department of Meteorology and Geophysics, University of Vienna, Vienna, Austria

9

10 **Abstract**

11 The Arctic is experiencing unprecedented moistening which is expected to have far-reaching impact
12 on global climate and weather patterns. However, it remains unclear whether this newly-sourced
13 moisture originates locally from ice-free ocean regions or is advected from lower latitudes. In this
14 study, we use water vapour isotope measurements in combination with trajectory-based diagnostics
15 and an isotope-enabled AGCM, to assess seasonal shifts in moisture sources and transport pathways
16 in the Arctic. Continuous measurements of near-surface vapour, $\delta^{18}\text{O}$, and δD were performed
17 onboard RV Polarstern during the MOSAiC expedition from October 2019 to September 2020.
18 Combining this isotope dataset with meteorological observations reveals that the spatiotemporal
19 evolution of $\delta^{18}\text{O}$ mimics changes in local temperature and humidity at synoptic to seasonal time
20 scales, while corresponding d-excess changes suggest a seasonal shift in the origin of moisture.
21 Simulation results from the particle dispersion model FLEXPART support these findings, indicating
22 that summer moisture originates from nearby open ocean, while winter moisture comes from more
23 remote sources with longer residence time over sea-ice. Results from a nudged ECHAM6-wiso
24 simulation also indicate that evaporative processes from the ocean surface reproduce summer
25 isotope values, but are insufficient to explain measured winter isotope values. Our study provides
26 the first isotopic characterization of Central Arctic moisture over the course of an entire year, helping
27 to differentiate the influence of local processes versus large-scale vapour transport on Arctic
28 moistening. Future process-based investigations should focus on assessing the non-equilibrium
29 isotopic fractionation during air mass transformation over sea-ice.

30

31 **Plain language abstract**

32 The Arctic is warming twice as fast as the world's average and its water cycle is undergoing large
33 changes. The Arctic atmosphere is becoming more humid; however, it is unclear whether the
34 moisture is sourced locally from ice-free ocean regions or if the vapour is transported into the Arctic
35 from lower latitudes. To assess the origin of the moisture, we use the isotopic composition of water
36 vapour obtained onboard a research icebreaker drifting across the Central Arctic ocean. Our
37 observations indicate that the spatial-temporal evolution of $\delta^{18}\text{O}$ follows the changes in local
38 temperature and humidity. The corresponding deuterium excess signal, which is used as a diagnostic
39 of moisture source conditions, suggests a seasonal shift in the origin of the air masses. Results from
40 a backward trajectory analyses and from an atmosphere general circulation model indeed show that
41 summer moisture originated from the ocean surface near the sampling site, while winter moisture
42 had a longer residence time over the sea-ice making it more prone to experience isotopic
43 fractionation along the transport. Future model simulations should assess the importance of in-cloud

44 microphysics and surface moisture exchanges in winter, while additional field observations are
45 needed to reduce the uncertainties on the isotopic data.

46

47 **Key points**

- 48 • We present a year of atmospheric water vapour isotopes measurements obtained on a drift
49 cruise across the frozen Central Arctic ocean
- 50 • Summer moisture mostly originates from the open ocean and its isotopic composition
51 reflects source region's evaporative conditions
- 52 • ECHAM6-wiso cannot reproduce winter moisture's isotopic composition, suggesting non-
53 equilibrium exchanges during transport over sea-ice

54

55 **Index terms**

56 3339 ATMOSPHERIC PROCESSES/ Ocean-Atmosphere interactions

57 3349 ATMOSPHERIC PROCESSES/Polar meteorology

58 1833 HYDROLOGY/Hydroclimatology

59 1041 GEOCHEMISTRY/Stable isotope geochemistry

60 0750 CRYOSPHERE/Sea Ice

61

62 **Keywords**

63 Water isotopes, atmospheric water vapour, Arctic, water cycle, AGCM

64

65 1. Introduction

66

67 The Arctic is experiencing a rapid decline of sea-ice coverage and overall alteration of
68 atmospheric and oceanic circulation patterns (Fox-Kemper et al., 2021 in IPCC, 2021). Feedback
69 loops link changes in albedo, water vapour, cloudiness and heat fluxes resulting in an Arctic
70 amplification of the global warming (Holland and Bitz, 2003; Serreze and Barry, 2011; Vihma et al.,
71 2016). Local changes in the Arctic may cause extreme mid-latitude weather events (Cohen et al.,
72 2014) and are also linked to the global climate system by large-scale teleconnections (Huang et al.,
73 2017). Yet the consequences of the changing Arctic remain uncertain due to paucity of observational
74 data and large spread in model projections (Cohen et al., 2020; Ye and Messori, 2021).

75 Amongst other hydrological changes, a significant increase in the atmospheric specific humidity has
76 been observed in the Arctic in the last two decades (Vihma et al., 2016; Rinke et al., 2019). Whether
77 this additional moisture is locally recycled as a result of an intensified hydrological cycle within the
78 Arctic region itself or is the result of changes in magnitude, distribution and seasonality of regional
79 atmospheric moisture transport, is to date still uncertain. Most studies attribute the moistening of
80 the Arctic atmosphere to northward advection (Zhang et al., 2013). Global warming leads to higher
81 moisture content in the atmosphere and stronger meridional moisture gradients (Bengtsson et al.,
82 2011). Rising temperatures are also expected to cause the poleward migration of the sub-polar
83 westerly jet stream and the intensification of storm-tracks. Hence, more moisture is able to converge
84 into the Arctic region without intensification of the local hydrological cycle. However, conflicting
85 results were reported on the actual frequency of such events in the recent decades (Zahn et al., 2018).
86 In contrast to the advection hypothesis, modelling studies suggest that, under the current warming
87 conditions, the Arctic moisture and consequent precipitation will increase due to intensified local
88 surface evaporation and only to a lesser degree due to enhanced moisture inflow from lower latitudes
89 (Bintanja and Selten, 2014; Bintanja 2018). While the increase of latent heat release in areas of
90 reduced sea-ice extent in winter (Kopec et al., 2016) is undisputed, its contribution was found to be
91 confined to specific regions (Rinke et al., 2019) and seasons (Kurita et al., 2011). Hence, there are
92 doubts on the contribution of surface fluxes on the overall moistening and hydrological sensitivity of
93 the changing Arctic.

94 Water stable isotopologues (H_2^{16}O , HD^{16}O , H_2^{18}O , hereafter referred to as water isotopes) are
95 valuable atmospheric tracers because of the various fractionation processes occurring at phase
96 transition and during diffusive vertical vapour transport in the near-surface atmosphere (Urey,
97 1947). Water bodies that undergo evaporation become enriched in heavy isotopes, while air masses
98 cooling during poleward transport experience depletion due to the removal of heavy isotopes during
99 progressive rainout. Such (a-)diabatic cooling can be described by a Rayleigh model (Craig, 1961).
100 This type of fractionation, dependent on differences in saturation vapour pressure, is referred to as
101 equilibrium fractionation, the strength of which is inversely related to temperature. A different type
102 of fractionation occurs when the phase change is not in equilibrium, such as during evaporation
103 (Dansgaard, 1964; Craig and Gordon, 1965). The difference in diffusion velocity between D/H and
104 $^{18}\text{O}/^{16}\text{O}$ alters the diffusion rates of the respective water molecules in the air (Merlivat 1978,
105 Hellmann and Harvey 2020). The second-order isotope parameter, deuterium excess ($d\text{-excess} = \delta\text{D}$
106 $- 8 * \delta^{18}\text{O}$; Dansgaard, 1964), describes the magnitude of such non-equilibrium fractionation.

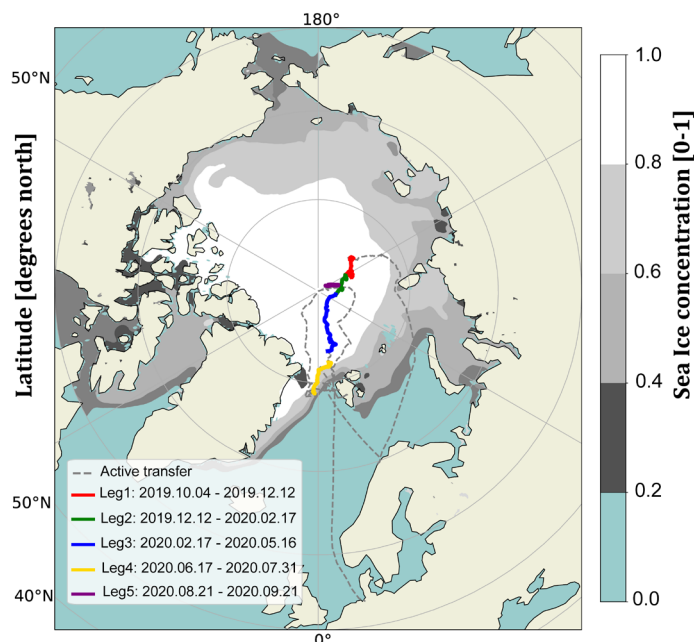
107 Stable water isotopes have made significant contributions to deciphering hydroclimatic processes in
108 the Arctic. An important contribution consisted in the attribution of specific isotopic signatures to air
109 masses originating at different latitudes (Bonne et al., 2014,2015,2020; Steen-Larsen et al., 2015;

110 Leroy Dos Santos et al., 2019). Another area of focus has been on studying the evolution of the
111 isotopic signature of the surface snow during post-depositional processes, which change the isotopic
112 composition of snow through sublimation and solid-condensation (Wahl et al., 2022). This
113 knowledge is not only key for the interpretations of past climate variability in ice-core records;
114 comparisons of measured and modelled water vapour isotopes suggest that snow sublimation in sea-
115 ice covered regions depletes the atmospheric water vapour in $\delta^{18}\text{O}$ and increases the d-excess (Bonne
116 et al., 2019). Additionally, d-excess was suggested to be a proxy for sea-ice extent (Klein et al., 2016),
117 due to the coupled strong distillation during the transport and the non-equilibrium evaporative
118 contribution from leads into the atmosphere. Recently, water isotopes have been used to link in-
119 Arctic sourced moisture to extreme snowfall over northern Europe, highlighting a connection
120 between the changing Arctic and the mid-latitude precipitation regimes (Bailey et al., 2021).

121 Most of the mentioned studies use land-based observations from coastal stations. However,
122 coastlines are not representative for the climate dynamics occurring at higher latitudes where open
123 ocean, sea-ice and snow, co-exist and exchange dynamically through the year. For a long time, the
124 harsh winter conditions, and large extent of concentrated sea-ice had limited ship-based campaigns
125 and fully prevented observations of the winter conditions. This limitation persisted until 2019, when
126 the Multidisciplinary drifting Observatory for the Study of Arctic Climate (MOSAiC) drift experiment
127 (Shupe et al., 2020) offered the unique possibility to address the main hydrological processes
128 occurring in the Central Arctic, covering a complete seasonal cycle including the understudied Arctic
129 winter. From October 2019 to September 2020 the research vessel RV Polarstern (POL) drifted
130 passively across the Central Arctic enabling a cross-disciplinary crew to conduct comprehensive
131 observational and sampling activities. The MOSAiC drift was articulated into five phases, so called
132 'legs', interjected by personnel rotation, supplies and in some cases active navigation transit for
133 repositioning (Figure 1).

134 In this study, we investigate the atmospheric water cycle and the moisture source changes during the
135 MOSAiC drifting campaign. We present the first complete annual observation dataset of near-surface
136 atmospheric water vapour isotopes (δD and $\delta^{18}\text{O}$) in the Central Arctic. To disentangle local and
137 regional processes, we estimate the atmospheric moisture sources based on Lagrangian backward
138 trajectories. To assess whether climate models successfully capture such local and regional moisture
139 exchange processes, we compare our observations to the results of a simulation from a state-of-the-
140 art atmosphere general circulation model (AGCM) equipped with explicit water isotopes diagnostics
141 and nudged to meteorological analyses.

142



143
 144 Figure 1: Drift track of RV Polarstern during the Multidisciplinary drifting Observatory for the Study of Arctic Climate
 145 (MOSAIC). The total drift is coloured based on the different expedition phases (legs). Active ship movement is illustrated by
 146 a grey dashed line. Average sea-ice concentration during the campaign (from ECMWF) is coloured in scale of greys.

147

148

149 2. Data and Methods

150

151 2.1 Atmospheric water vapour isotopes

152

153 Amongst a large range of other atmospheric observations (Shupe et al. 2022), continuous, in-situ
 154 measurements of stable water isotopes were obtained from a Picarro L2140-i CRDS operated during
 155 the entire campaign (Brunello et al., 2022a,b,c,d,e). The ambient air inlet was located on the P-Deck,
 156 at 29 m above sea level (asl), and connected to the CRDS analyser by a 25 m long stainless-steel tube,
 157 heated at 63°C to avoid condensation. The line was pumped with a KNF N 86 KT.18 pump, and the
 158 flow rate was about 5 l/min. Raw data of humidity mixing ratio, $\delta^{18}\text{O}$ and δD were obtained at the
 159 temporal resolution of 1 Hz. The raw isotopic data ($\delta^{18}\text{O}$ and δD) obtained from the CRDS were
 160 corrected and calibrated using the same custom-made system and correction procedure as described
 161 in Bonne et al., 2019. Four different liquid isotopic standards of known isotopic composition were
 162 vaporized and injected into the analyser for 30 min every 25 h. Calibration curves were calculated
 163 based on the linear regression of the 14-day running average of each standard measurement vs
 164 VSMOW and used to correct the ambient measurements. Further, analysers need to be characterized
 165 for the response of the measured isotopic values as a function of water vapour concentration. To
 166 account for this, prior to the expedition, each isotopic standard besides one, was measured over a
 167 range of controlled humidity levels and the results were interpolated with a polynomial function of
 168 fourth order (Figure S1). No humidity correction function was available for the most depleted
 169 standard. Details about the calibration routine and the empirical corrections can be found in the
 170 supplements (Text S1). We found that analytical uncertainties calculated at 1 h resolution are higher
 171 during winter, peaking in March (1.1‰, 5.2‰, 10‰, for $\delta^{18}\text{O}$, δD and d-excess respectively) and

172 represent an important, yet unavoidable caveat for this study. Most (84.8%) of the winter (DJFM)
173 observations occurred below 0.4 g/kg, the lowest humidity level for which humidity-response
174 measurements were available (details in Text S2). The entire dataset is presented here, but
175 interpretation of the results at humidity levels below 0.4 g/kg will consider increased uncertainties
176 and when relevant the corresponding data are illustrated with a different marker.

177

178 *2.2 Meteorological data*

179

180 The local meteorological data used in this study were routinely measured on POL. The related
181 sensors are located at different heights: relative humidity (RH) and air temperature (T) at 29 m above
182 sea level; air pressure (p) is measured at an altitude of 19 m, but expressed at sea level. Specific
183 humidity (q) is calculated based on RH, T and p. The calibrated and validated datasets are available
184 at a 1-min averaged temporal resolution on PANGAEA (Schmithuesen, 2021).

185 Gridded near-surface meteorological parameters based on the European Centre for Medium-range
186 Weather Forecasts (ECMWF) fifth-generation reanalysis (ERA5) reanalysis dataset (Hersbach et al.,
187 2023) are used to characterize the spatial sensitivity of the isotope measurements to the
188 environmental conditions during the MOSAiC year. These parameters include single-level variables
189 such as sea surface temperature (SST), 2 m air temperature (T2m), skin temperature (T_{skin}), surface
190 pressure (SP), 2 m specific humidity (Q2m) obtained from 2 m dewpoint temperature, and sea-ice
191 concentration (SIC). All variables were extracted at 1h resolution. The relative humidity with respect
192 to the skin temperature (RH_{skin}) was calculated as the ratio of specific humidity divided by the
193 saturation specific humidity at skin temperature. Our RH_{skin} is equivalent to the relative humidity
194 with respect to sea surface temperature over the open ocean, however, the use of RH_{skin} allows to
195 extend the calculation over ice-covered regions.

196

197 *2.3 FLEXPART simulation and moisture source diagnostic*

198

199 To gain insights into the source regions of sampled water vapour, we used the Lagrangian particle
200 dispersion model FLEXPART (Stohl et al., 2005, Pissot et al., 2019). The model was driven with hourly
201 data from ERA5. Every 3 h, 100,000 atmospheric particles were initialized in a 0.1°×0.1°×100 m box
202 around POL and traced backward for 30 days. The gridded output of this back-trajectory simulation
203 represents the residence time (s) of air masses over the geographic grid cell during their transport.
204 Time series of residence time close to the surface (below 100m altitude, the lowest model output
205 layer) in the last 10 days before arrival were integrated over 6 distinct regional sectors (Asia, Europe,
206 North America, Greenland, open ocean, sea-ice, Figure S2) to show the relative influence of these
207 domains on the atmospheric composition observed at POL year-round.

208 The backward trajectories were used to identify the source regions of the vapour sampled and
209 measured during MOSAiC based on the diagnostic originally proposed in Sodemann et al. (2008) and
210 subsequently applied on FLEXPART trajectories in Sodemann and Stohl (2009). This moisture source
211 diagnostic is now referred to as WaterSip (Fremme and Sodemann, 2019). WaterSip version 2.8.1
212 (Bonne et al., 2014) is used to estimate the source regions. The humidity budget of an air parcel is
213 defined as the difference between evaporation (E) and precipitation (P), and WaterSip assumes that
214 at each 3 h time step either E or P dominates while the other can be ignored. Evaporation and
215 precipitation are estimated by integrating the humidity budget (Δq) along each individual trajectory
216 arriving at the position of POL. Increases in specific humidity in the air parcels exceeding the
217 threshold value of 0.1 g kg⁻¹ 3h⁻¹ are assumed to result from evaporation, sublimation or

218 transpiration from the surface, whereas decreases are attributed to precipitation. At each time step,
219 the fractional contribution of a humidity increase is calculated. In case of precipitation, previous
220 evaporation regions are assumed to contribute proportionally to the fraction they represent in the
221 air parcel. When part of the humidity of an air parcel precipitates, all earlier evaporative
222 contributions are thereby reduced accordingly. Eventually, WaterSip provides a fractional
223 contribution of “moisture uptake” (in mm/timestep) on a $0.5^\circ \times 0.5^\circ$ grid of each evaporation event to
224 the moisture sampled in the target area. Note that the magnitude of the moisture uptakes depends
225 on the size of the release box. We therefore focus on the relative spatial and temporal differences
226 rather than the absolute variability of the moisture uptakes.

227

228 *2.4 Water isotope simulation with ECHAM6-wiso*

229

230 A simulation of the atmospheric water vapour isotope composition was performed with the isotope-
231 enabled atmospheric model ECHAM6-wiso. ECHAM6 is the sixth generation of the atmospheric
232 general circulation model ECHAM, developed at the Max Planck Institute for Meteorology (Stevens et
233 al., 2013). The different water isotopes are treated as inert tracers for atmospheric transport
234 processes in ECHAM6-wiso. Changes of the isotopic composition of an air parcel can thus only occur
235 due to mixing of air masses with different isotopic signatures. Kinetic fractionation processes are
236 included for evaporation of ocean surface water, the formation of snow at low temperatures as well
237 as for the partial re-evaporation of raindrops and snow falling through an undersaturated
238 atmosphere (Cauquoin et al., 2019). Two of the most prominent updates in respect to ECHAM5-wiso
239 (Werner et al., 2011) are related to the isotopic composition of snow-covered sea-ice and the
240 evaporation over ocean, as suggested and parameterized in Bonne et al. (2019). First, the isotopic
241 composition of vapour over sea-ice covered areas is now affected by the isotopic composition of the
242 snow layering on the sea ice surface. Hence, snow sublimation, assumed to happen without
243 fractionation, can deplete the atmospheric water vapour $\delta^{18}\text{O}$ and increase the d-excess of the near-
244 surface water vapour. Second, instead of applying the wind speed dependency of the kinetic
245 fractionation factor proposed by Merlivat and Jouzel in 1979, a constant kinetic fractionation factor
246 is applied (Benetti et al., 2014).

247 In this study, we present the results from a single model simulation performed at a horizontal grid
248 size of $\sim 0.9 \times 0.9^\circ$ and 95 vertical levels (T127L95). To ensure that the simulated large-scale
249 atmospheric flow is modelled in agreement with the ECMWF reanalysis data, the model is nudged to
250 ERA5 surface pressure, temperature, vorticity and divergence fields (Butzin et al., 2014). For each
251 model output time step (6 h), the simulated water vapour amount and its isotopic composition are
252 extracted from the near-surface model grid cell encompassing the position of POL along the MOSAiC
253 drifting track. In the vertical direction, this near-surface grid cell extends from the surface to ~ 60 m
254 above the surface.

255

256

257 **3. Results**

258 In the following section, we present the results of our investigation of atmospheric stable water
259 isotopes measured during the MOSAiC expedition in the central Arctic Ocean. It is important to note
260 that the observed changes are not solely driven by seasonal variations; they also reflect fluctuations
261 caused by the drifting cruise and relocations of RV Polarstern (POL). Therefore, the patterns we
262 discuss are the combined result of both spatial and temporal factors. Throughout this manuscript,

263 the significance of the correlation analyses is assessed using p-values. Unless stated otherwise, all
264 correlations reported in this study have p-values below 0.01.

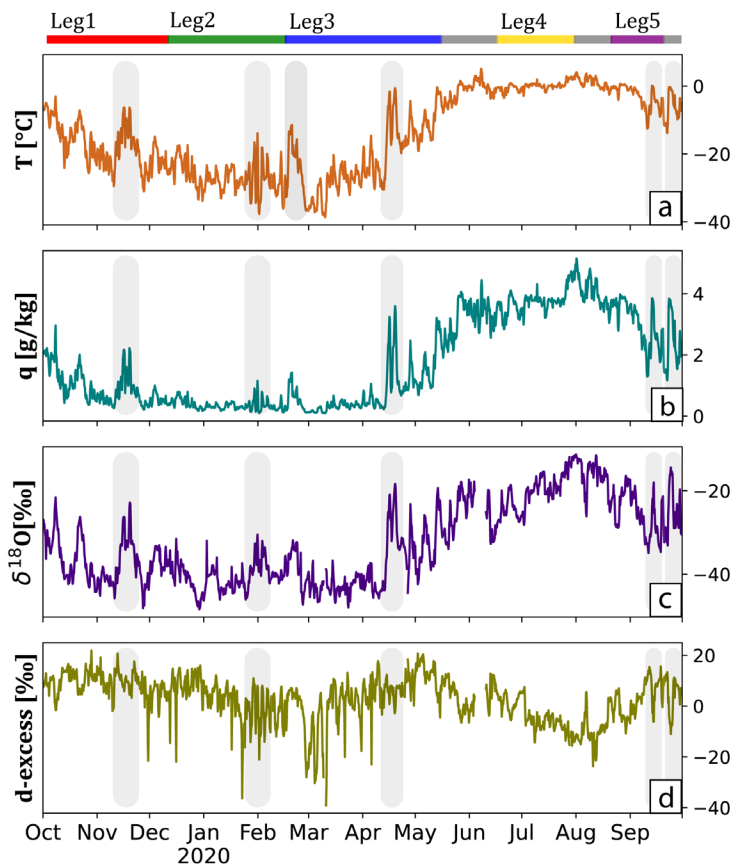
265
266

267 3.1 Water vapour isotope variations at RV Polarstern during the MOSAiC expedition

268

269 The calibrated data of water vapour $\delta^{18}\text{O}$ and δD from the Picarro CRDS, and the related time series
270 of specific humidity (q) and air temperature (T) measured routinely as part of the meteorological
271 observations on POL are displayed in Figure 2.

272



273

274 Figure 2: From top to bottom: (a) temperature, (b) humidity, (c) $\delta^{18}\text{O}$, and (d) d-excess of atmospheric water vapour
275 measured at 19m on the mast of RV Polarstern during the MOSAiC drifting expedition in the Central Arctic, aggregated here
276 at 6 h resolution. The time span of each phase of the expedition (named legs, Fig.1) is illustrated in the upper bar, the active
277 transfer of RV Polarstern is shown as a grey phase. Vertical shaded grey bars in panels (a)-(d) mark the occurrence of
278 synoptic warm air intrusions.

279 The dataset spans from October 1st, 2019 to September 30th, 2020 and includes a total of 7564
280 hourly data points, accounting for 86% of a full annual cycle. Gaps in the water isotope data exist due
281 to the removal of outliers related to instable measurements of the Picarro instrument (details in S1).
282 Furthermore, vapour data were not collected from June 03 to June 08 when POL entered the Svalbard
283 territorial waters and atmospheric measurements were not permitted.

284 Aggregated to a 3 h resolution, temperature and humidity values over the course of the MOSAiC
285 expedition year range between $-38.8\text{ }^{\circ}\text{C}$ to $5.2\text{ }^{\circ}\text{C}$ (mean: $-14.3\text{ }^{\circ}\text{C}$, std: $11.8\text{ }^{\circ}\text{C}$) and 0.1 g/kg to 5.1
286 g/kg (mean: 1.7 g/kg , std: 1.4 g/kg), respectively. The $\delta^{18}\text{O}$ dataset ranges from a minimum of -49‰

287 to a maximum of -11.3‰ (mean: -32.3‰, std: 9.7‰), while the d-excess data series spans a wide
288 range of values, with a minimum of -46.5‰ and a maximum of 24.5‰ (mean:2.5‰, std:8.9‰).
289 Temperature, specific humidity, and $\delta^{18}\text{O}$, show a seasonal cycle in the data series, with low values in
290 the boreal winter (December–March) and high values during the boreal summer (June–September).
291 The seasonal changes of these three variables are correlated. On the opposite, no clear seasonal cycle
292 is observed for the d-excess values, which show a high variability throughout the entire winter time
293 and a decreasing trend from May to September, in antiphase with the summer $\delta^{18}\text{O}$ values.
294 Several positive $\delta^{18}\text{O}$ excursions are observed on a sub-seasonal, synoptic time scale, coinciding with
295 maxima in both local temperature and specific humidity (Figure 2, vertical grey bars). Most of these
296 excursions can be identified as the local expression of warm intrusions carrying moist air masses
297 from mid-latitudes poleward into the Central Arctic (Rinke et al. 2019). These events are more
298 noticeable in winter and autumn. Typically, such passage of extratropical cyclones and their
299 associated warm (cold) sectors leads to positive (negative) anomalies of $\delta^{18}\text{O}$ in anticorrelation with
300 changes in d-excess (Dütsch et al., 2016, Thurnherr et al., 2021). In all cases of our data set, warm air
301 intrusions led indeed to an increase in $\delta^{18}\text{O}$ and a matching decrease in d-excess, except for the events
302 in December and February, where the d-excess values were increasing, too. In addition, extreme
303 negative d-excess excursions with no counterpart of positive $\delta^{18}\text{O}$ changes are observed both in
304 wintertime (with strongest negative excursions between mid-February and mid-March) and
305 summertime (July and August). No daily cycles were observed at any time during the observational
306 period, neither in the vapour isotopic composition nor in the air temperature and humidity. The lack
307 of diurnal variability implies that the moisture measured on board POL is not influenced by diurnal
308 changes in local radiation, surface fluxes and boundary layer mixing and that the synoptic and
309 seasonal changes dominate the records.

310
311

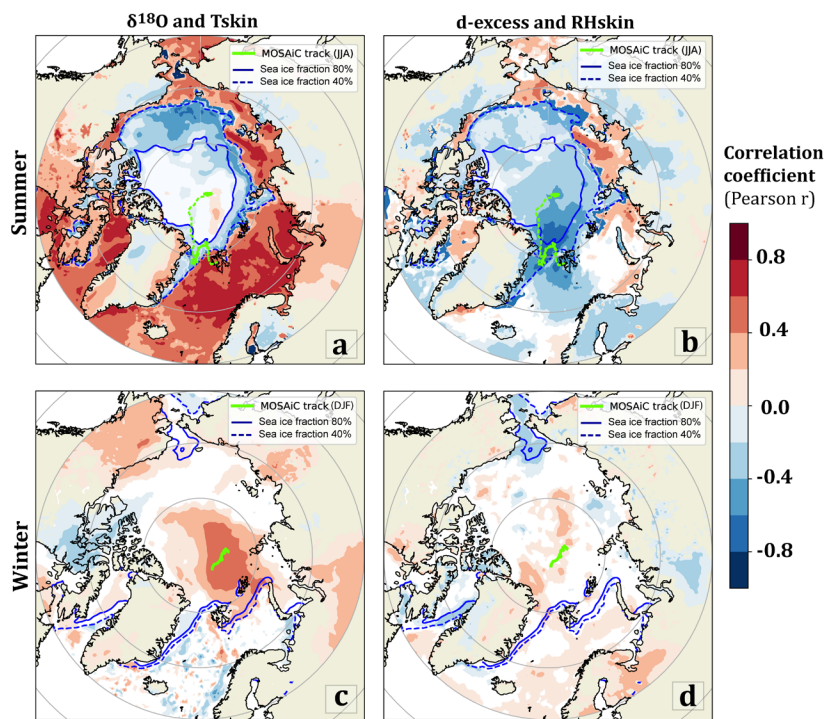
312 *3.2 Linking RV Polarstern vapour data with regional surface temperature and humidity changes*

313

314 In order to explore the linkage of the water vapour isotopes to environmental variables at the
315 regional scale, correlation analyses were conducted using the gridded meteorological reanalysis data
316 from ERA5. These maps are especially relevant for the identification of evaporative source regions,
317 which might differ from the conditions at the sampling site. While variations in surface temperature
318 lead to changes in evaporation from water bodies influencing the $\delta^{18}\text{O}$ composition, relative humidity
319 with respect to surface temperature is a driving factor for kinetic fractionation (Pfahl and Wernli,
320 2008). Figure 3 shows seasonal mean correlation values of $\delta^{18}\text{O}$ with T_{skin} and d-excess with RH_{skin} ,
321 respectively.

322 During summer, the water vapour $\delta^{18}\text{O}$ variations correlate positively with T_{skin} over the open ocean
323 (Fig. 3a). These correlations are spatially unselective and cover most of the ocean sector, which
324 indicates that seasonal temperature changes in the Arctic are spatially coherent for most regions. An
325 opposite, but weaker correlation is found in the mixed sea ice-open ocean sector north of Alaska and
326 Siberia. Correlation values over the sea-ice area are low and largely non-significant as opposed to
327 winter (Fig. 3c), where a positive correlation pattern is observed over the frozen Central Arctic
328 Ocean. The summer d-excess variations correlate negatively with the RH_{skin} over the Central Arctic
329 Ocean (Fig. 3b), with the highest values found in the Greenland Sea, straddling the margin of the sea-
330 ice. Positive correlation is observed over the open ocean along the Siberian coast and Bering Strait.

331 Positive significant correlation is also found between d-excess and RH_{skin} over the sea-ice in winter
 332 (Fig. 3d), although correlation values are low and without a consistent spatial pattern. Low
 333 correlation is also observed in the Atlantic Ocean, Scandinavia and Bering Strait.
 334



335
 336
 337 *Figure 3: Seasonal correlation maps (Pearson's r at 99.9% confidence interval) of water vapour $\delta^{18}O$ and skin temperature*
 338 *T_{skin} (a,c) and d-excess and relative humidity RH_{skin} (b,d). Panels a and b show the Arctic summer (JJA), c and d the winter*
 339 *season (DJF). The blue lines mark the area of sea fraction higher than 80% (solid) and 40% (dashed), respectively. Correlation*
 340 *coefficients were calculated based on the 3 h resolution track data sets at all locations north of 60°N, assuming no time lag.*
 341

342 These results suggest distinct moisture sources for summer and winter conditions. In summer, the
 343 strong positive correlation between $\delta^{18}O$ in vapor and temperature variations over the ice-free North
 344 Atlantic and Barents Sea suggests moisture uptake from these regions. Additionally, d-excess
 345 indicates that especially uptake from the sea-ice margin plays a role in modulating the non-
 346 equilibrium fractionation of summer moisture. In contrast, during winter, water vapour $\delta^{18}O$ and d-
 347 excess, correlates primarily with temperature and humidity changes over sea-ice-covered areas. This
 348 may suggest either a contribution from locally recycled moisture or a superposition of the primary
 349 oceanic evaporation signal by additional fractionation processes during the transport of vapour over
 350 sea-ice in winter. However, the complex correlation patterns of d-excess do not allow more precise
 351 conclusions here.

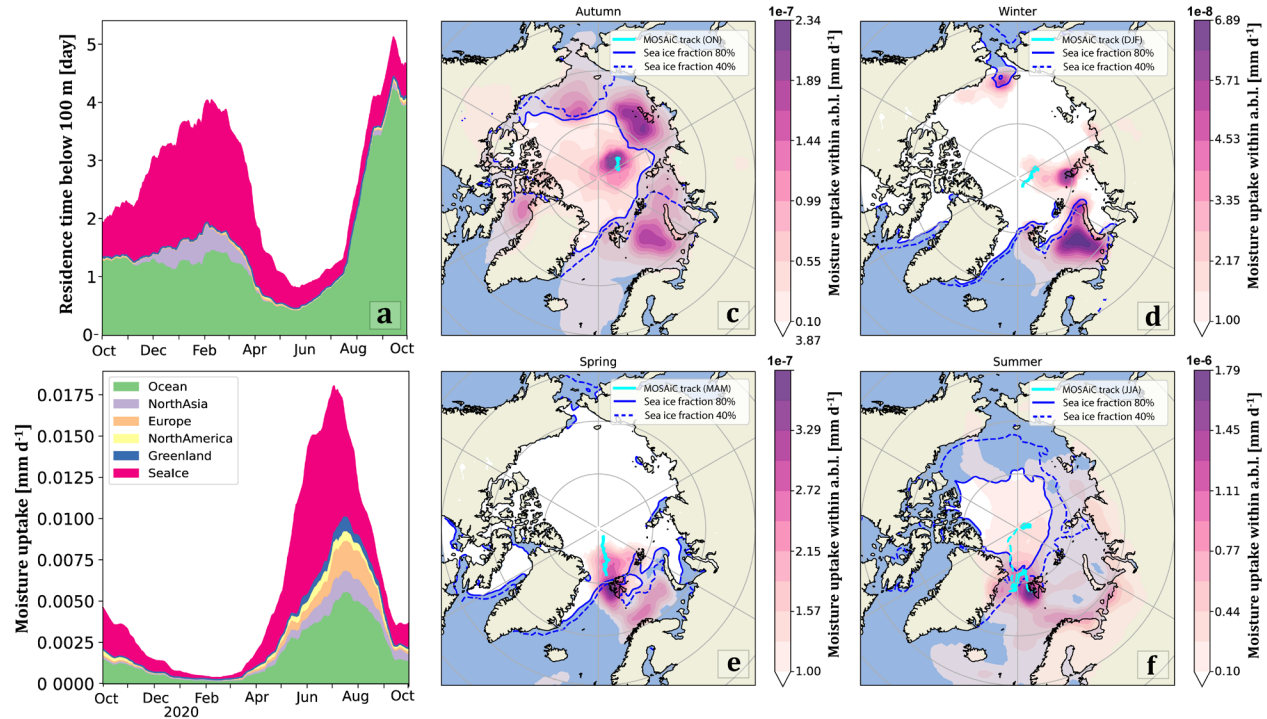
352 3.3 Trajectory-based moisture source diagnostic

353
 354
 355 In order to further investigate the influence of changes in moisture source regions on the isotopic
 356 composition of the water vapour, we applied a moisture source diagnostic to the backward air
 357 trajectory simulations obtained from the FLEXPART atmospheric transport model. Note that the

358 absolute values are low as they represent the contribution of the moisture content within a small
359 release box (Sec. 2.3).

360 The average moisture uptake in millimetres per day for each calendar season, is illustrated in Figure
361 4. Our findings show that the moisture sources of the vapour measured at POL during the MOSAiC
362 campaign varied from season to season, both in location and strength (Fig. 4a, b). Strong evaporation
363 from different source regions associated with short residence times is taking place in summer (June-
364 Aug) and low evaporation associated with longer residence times in the late winter (Feb-April).
365 These seasonal differences in evaporation strength are reflected in the corresponding variations in
366 specific humidity at POL (Fig. 2).

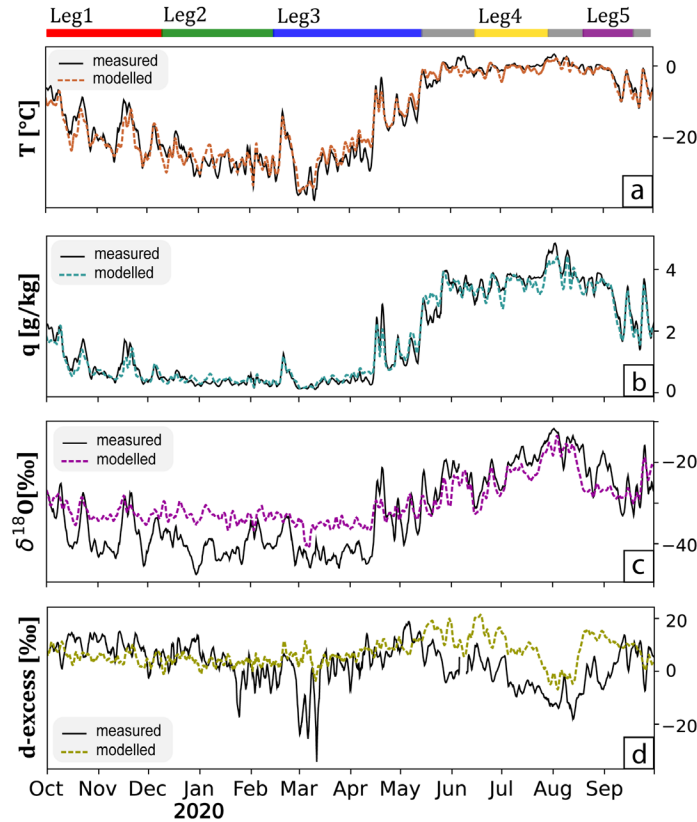
367 With regard to the key moisture source regions, in autumn, at the beginning of the MOSAiC
368 expedition, predominantly moisture from the Arctic Ocean was transported to POL (Fig. 4c). Three
369 main source regions could be identified: (i) the area surrounding POL, which is fully covered by sea-
370 ice; (ii) the sea-ice margin over the Laptev, Eastern Siberian and Beaufort Seas, where sea-ice
371 concentration is on average lower and mixed conditions of open ocean and growing sea-ice can be
372 found and (iii) the ice-free Barents Sea. In winter, the overall moisture uptake decreases, the uptake
373 over sea-ice covered areas vanishes and the only remaining moisture source is the ice-free Barents
374 Sea (Fig. 4d). During spring, while POL drifted southward across the Arctic Ocean, moisture uptake
375 increased again and the moisture uptake region extended from the Barents Sea westward to Svalbard
376 and the Greenland Sea (Fig. 4e). This shift might be partly also caused by the more southern position
377 of POL. This season marks a transition from winter conditions with large sea-ice areas to melting
378 conditions with retreating sea-ice areas. In summer, moisture uptake is at its seasonal maximum (ca.
379 0.017 mm d^{-1}). The moisture source region covers a large sector of the Arctic ocean, with the most
380 prominent contribution from the southern and western coasts of Svalbard, surrounding POL.
381 Additional contribution is provided from the Central Arctic and the Eurasian coastal regions. The
382 wide distribution of moisture sources can be attributed both to warmer temperature and larger
383 availability of liquid water, and to the spatial variability in sampling, due to the relocation of POL
384 from Leg 4 to Leg 5 (Fig.1). In Figure S3, we present the moisture uptakes of each Leg separately.
385 Both Leg 4 and 5 experienced large spread in moisture source locations with significant contribution
386 from the open ocean. However, during Leg 4, POL primarily received moisture from the west of
387 Svalbard, whereas during Leg 5, the majority of the moisture originated from the Laptev Sea. These
388 two patterns combine to form the average summer (JJA) moisture uptake map.



389
 390 *Figure 4. Left panels: 60-day running average of (a) residence time below 100 m obtained from the FLEXPART model and (b)*
 391 *moisture uptake under the atmospheric boundary layer (a.b.l) from the WaterSip diagnostic, computed along the MOSAIC track*
 392 *and aggregated over distinct regions. Right panels: regional maps with seasonal averages of boundary layer moisture uptake (mm*
 393 *d⁻¹). The solid cyan line marks the seasonal track of RV Polarstern, the blue lines mark the area of sea-ice fraction higher than 80%*
 394 *(solid) and 40% (dashed).*

395
 396 **3.4 Comparison of RV Polarstern measurements with ECHAM6-wiso simulation results**
 397

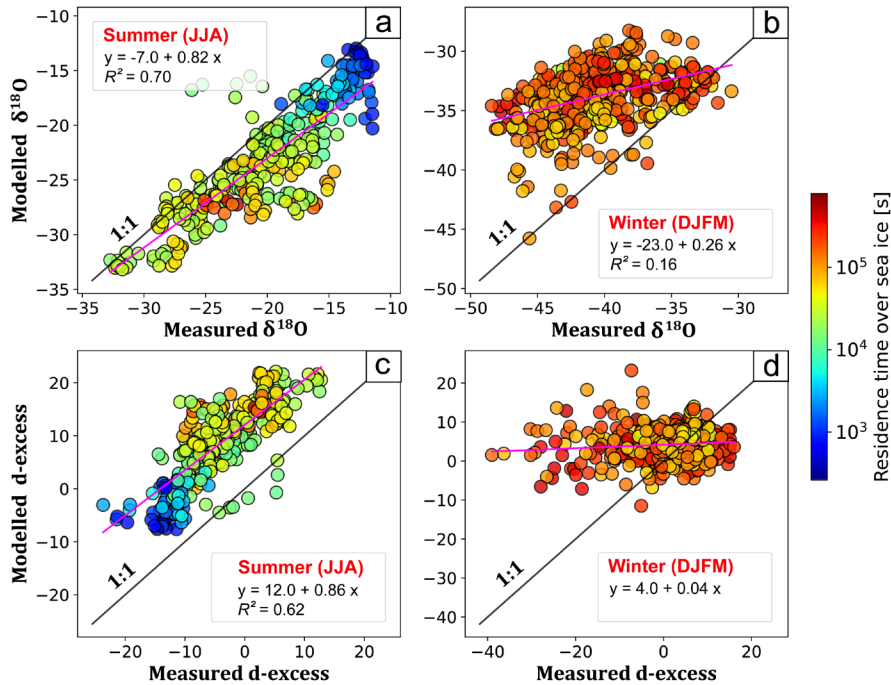
398 To gain further understanding of the observed isotopic changes, and to assess whether an AGCM
 399 reproduces these changes, we compare the isotopic and meteorological observations from MOSAIC
 400 (Fig. 2) with model results from a nudged ECHAM6-wiso atmospheric simulation (Sec. 2.4).
 401 The modelled air temperature changes (Fig 5a) match closely the observations ($r^2=0.94$) because in
 402 this ECHAM6-wiso simulation the modelled 3D-field of temperature was nudged toward ERA5
 403 reanalysis data every 6 h. In contrast, none of the hydrological variables in the ECHAM model were
 404 nudged, to allow a physically consistent interpretation of the simulated water vapour isotope values.
 405 Nevertheless, simulated humidity changes (Fig 5b) are in very good agreement with the observations
 406 as well ($r^2=0.96$). This is true for both the mean levels, and on a seasonal and synoptic time scale.
 407



408
 409 *Figure 5: Time series (from 1 October 2019 to 30 September 2020) of ECHAM6-wiso model results of the nearest surface grid box,*
 410 *and observations along the track of RV Polarstern during MOSAiC. The subplots report modelled and measured a) air temperature*
 411 *(°C); b) water vapour specific humidity (g kg⁻¹); c) water vapour δ¹⁸O (‰) and d) water vapour d-excess (‰). All values are*
 412 *averaged over a moving window of 48h.*

413
 414 Despite the good agreement of the specific humidity values, larger discrepancies are found between
 415 modelled and measured water vapour isotopes. For δ¹⁸O (Fig. 5c), ECHAM6-wiso overestimates the
 416 absolute values of δ¹⁸O in winter and early spring (Oct-April) by 6.8‰ (mean difference of the 6 h
 417 aggregated datasets). Between mid-April and end of June modelled δ¹⁸O values match the measured
 418 ones. In summer (July-Sept) the simulated values are lower than the observations, with an average
 419 bias of 2.9‰. For d-excess (Fig 5d), simulated values are lower at the beginning of the winter season
 420 (Oct-Jan), but higher at the end of the winter (mid-Jan to mid-March). Modelled and measured d-
 421 excess values match between mid-March and mid-May. Modelled values are then systematically
 422 higher between mid-May and September (mean difference of 12.4‰).

423 The relationships between modelled and measured δ¹⁸O and d-excess values for summer (JJA) and
 424 winter (DJF) are illustrated in detail in Figure 6. In summer, the correlation between modelled and
 425 observed δ¹⁸O is r²=0.70, with a slope of 0.82‰ ‰⁻¹, and a negative intercept of -7‰. Similarly, d-
 426 excess has a correlation of r²=0.62, slope of 0.86‰ ‰⁻¹ and intercept of 12‰.



427
 428 *Figure 6: Seasonal scatterplots illustrating the relationships between measured and modelled $\delta^{18}\text{O}$ (a,b) and d-excess (c,d) in*
 429 *summer (JJA, left) and winter (DJFM, right) respectively. The data are aggregated at 6 h time resolution and they are coloured in*
 430 *logarithmic scale based on the residence time (s) over sea-ice retrieved from the 10-day FLEXPART backward trajectories. Linear*
 431 *regressions are shown as pink solid lines.*

432 In winter, modelled and observed $\delta^{18}\text{O}$ display statistically significant but low correlation ($r^2=0.16$),
 433 and a slope of 0.26 ‰ ‰^{-1} . No correlation is observed for d-excess. In this season, the ECHAM6-wiso
 434 model is not able to reproduce neither the relative changes nor the absolute values of the isotopic
 435 measurements. To note, while residence time over the sea-ice during summer was on average 0.35
 436 days (max: 5.6, min: 0), during winter the average residence time was 1.92 days (max 9.5, min:0.23).

439 4. Discussion

441 4.1 Correlation of measured $\delta^{18}\text{O}$ variations with local temperature and humidity changes

442
 443 For the measured $\delta^{18}\text{O}$ variations in vapour on board of RV Polarstern (POL), linear relationships are
 444 found with both the observed local temperature ($R^2=0.82$) and specific humidity ($R^2=0.88$) (Figure
 445 7). The slope between vapour $\delta^{18}\text{O}$ and temperature is $0.74 \text{ ‰ } ^\circ\text{C}^{-1}$ when considering the full dataset
 446 (Fig. 7a). This relationship is not stable through the year: winter (DJF) values have a lower slope
 447 ($0.42 \text{ ‰ } ^\circ\text{C}^{-1}$, $R^2=0.31$), while the summer (JJA) slope is steeper ($1.34 \text{ ‰ } ^\circ\text{C}^{-1}$, $R^2=0.57$). The $\delta^{18}\text{O}$ versus
 448 temperature slope over the full record is higher than the ones observed in Ny-Ålesund ($0.62 \text{ ‰ } ^\circ\text{C}^{-1}$,
 449 Leroy-DosSantos et al., 2020), at Inuituut, in Southern Greenland ($0.37 \text{ ‰ } ^\circ\text{C}^{-1}$, Bonne et al., 2014)
 450 and in Siberia, at the Lena River delta ($0.44 \text{ ‰ } ^\circ\text{C}^{-1}$, Bonne et al., 2020). These latter relationships are
 451 comparable to the slope of our winter observations. The low latitude of Inuituut, and the prevailing
 452 dominant weather systems were invoked as a potential explanation for such a low slope, but the
 453 comparably low slopes observed at the Lena delta and along the drifting track of MOSAiC suggest that
 454 latitude-related processes are not key controls of the temperature-isotope sensitivity. The summer

455 observations from MOSAiC display the steepest linear slope ever observed in the region ($1.34\text{‰ }^{\circ}\text{C}^{-1}$), close to the one retrieved in north-western Greenland during three consecutive summers ($1.1\text{‰ }^{\circ}\text{C}^{-1}$; Steen-Larsen et al., 2013). A shift towards higher $\delta^{18}\text{O}$ values is observed across the 0°C . This threshold marks the transition from a sublimate to an evaporative mode, where mixed phases of frozen and liquid water co-exist. The different fractionation factors associated with phase changes between these multiple compartments (e.g., open ocean, melt ponds, snow; Majoube 1971; Merlivat and Jouzel, 1979; Ellehoj et al., 2013, Lamb et al., 2017) might be responsible for the large variations of $\delta^{18}\text{O}$ observed around 0°C .

463 A linear relationship is also observed between $\delta^{18}\text{O}$ and the local specific humidity ($R^2=0.88$, slope $6.3\text{‰ }(\text{g}/\text{kg})^{-1}$; Fig. 7b). Here, the winter observations sampled in the Central Arctic have a rather low correlation ($R^2=0.31$) due to the compressed range of humidity conditions and high variability in the isotope observations. The correlation increases in summer ($R^2=0.64$), as the POL drifted southward in the Greenland Sea. In contrast to previous studies from the region (Leroy-Dos Santos et al., 2020, Bonne et al., 2020, Bastrikov et al., 2014), our observations do not show a logarithmic relationship with the local specific humidity. Such logarithmic relationship would agree with a theoretical Rayleigh isotopic distillation of air mass evaporating at midlatitudes and transported to high latitudes (Gat, 1996). Thus, our dataset suggests that either the air masses did not experience intense distillation processes along their trajectories or the air masses underwent local recharge of moisture modifying the isotopic composition or mixing ratio.

474 From this comparison of $\delta^{18}\text{O}$ versus local temperature and humidity, our data indicate that, while local temperature and local humidity are drivers of isotopic changes in summer, this is only moderately the case in winter, when the data show a weaker relationship with both temperature and specific humidity. This suggests that source or transport processes, independent of local air conditions, may contribute to influence the winter $\delta^{18}\text{O}$ signal measured at POL.

479

480

481 *4.2 Measured d-excess changes in vapour and corresponding $\delta^{18}\text{O}$ variations*

482

483 *4.2.1 D-excess variations with respect to previous observations*

484 The measured d-excess values on board POL showed a large temporal variation during the period of the MOSAiC campaign. Especially the very low, negative d-excess values measured in both winter and summer seasons are remarkable (Fig.2 and Chapter 3.1). We cannot completely rule out measurement artefacts, especially for very low humidity conditions in winter (see supplements, Text S2 for details). We also note that our d-excess values are considerably lower than previous observations from the region. For example, a 4.5 year-long monitoring of atmospheric water vapour at Ny-Ålesund revealed an average d-excess of $14.0 \pm 7.4\text{‰}$ (Leroy-Dos Santos et al., 2020). However, such very low negative d-excess values have not only been measured in vapour by the Picarro CRDS, but also in snow samples taken in the vicinity of POL during the MOSAiC expedition (Mellat et al., 2022). Furthermore, negative d-excess values in Arctic water vapour have been reported before: Bastrikov et al. (2014) associated negative d-excess values to mixing of dew-fall and canopy liquids with the atmospheric water vapour. This mechanism does not apply to our Central Arctic dataset, though. Steen-Larsen et al., (2013) used a 1-d box model to attribute negative d-excess values in Icelandic water vapour (as low as -10‰) to an evaporative flux into an ideally isolated planetary boundary layer above the ocean. More recently, studies from controlled laboratory and field experiments (Hughes et al., 2021) reported negative d-excess values in snow as a result of non-equilibrium exchange processes with the atmosphere. Yet, quantitative transfer functions linking

500

501 snow and vapour are still missing and there is no consensus on the physical mechanisms that could
502 result in such negative d-excess values in the atmospheric water vapour. Finally, condensation in
503 supersaturated conditions, which occurs at low temperature, leads to strong non-equilibrium
504 fractionation during vapour deposition onto the ice crystal and also leads to low d-excess in the
505 remaining vapour (Bolot et al., 2013, Dütsch et al., 2019). Given the important role played by
506 diffusivity in water phase transitions during the formation of ice and mixed-phase clouds (Rogers,
507 1979), d-excess is also sensitive to in-cloud microphysical parameters such as freezing temperatures
508 and degree of supersaturation (Samuels-Crow et al., 2014).

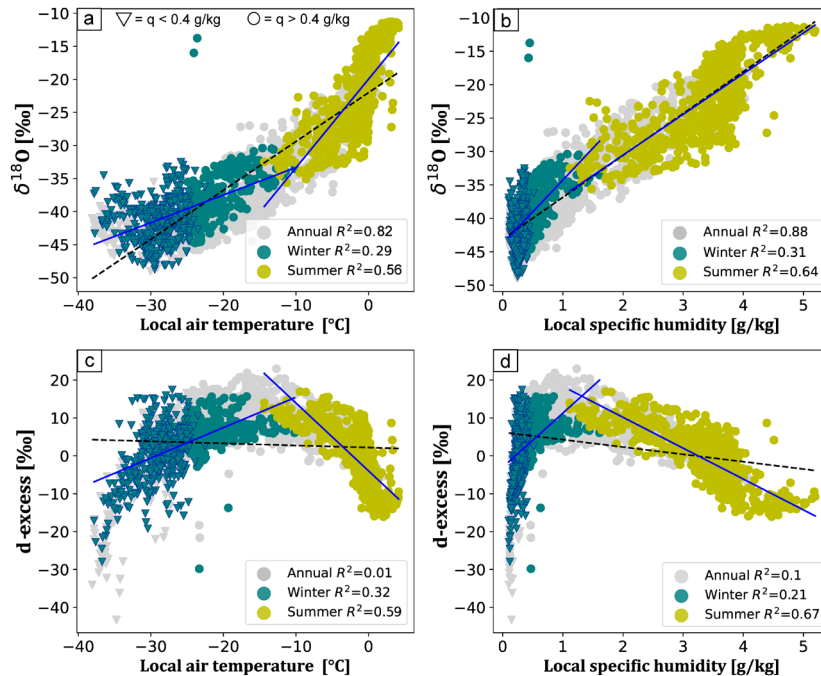
509

510 *4.2.2 D-excess variations with respect to $\delta^{18}\text{O}$ changes*

511 The negative d-excess values during the MOSAiC expedition are observed in two distinct seasons: in
512 wintertime characterized by extremely dry and cold conditions and in summertime at the maximum
513 of humidity and temperature levels (Figure 7c). Hence, there exists an anticorrelation between d-
514 excess and $\delta^{18}\text{O}$ in summer, but a positive correlation in winter. An anticorrelation was also
515 documented in Southern Greenland (Bonne et al., 2014), where a warm and moist summer was
516 characterized by $\delta^{18}\text{O}$ maxima and d-excess minima. This relationship has been interpreted as the
517 result of changes in the location of the moisture source region. Warm and moist events, with high
518 $\delta^{18}\text{O}$ and low d-excess, were associated with moisture originating at low latitudes such as south of
519 Greenland, as opposed to the moisture coming from the Iceland Sea or Davis Strait, characterized by
520 lower $\delta^{18}\text{O}$ and higher d-excess. On the other hand, the measured positive correlation between $\delta^{18}\text{O}$
521 and d-excess during MOSAiC in winter is in agreement with the positive correlation observed by
522 Leroy-Dos Santos et al. (2020). In this study, the authors investigated synoptic wet events during
523 winter at Ny-Ålesund and found that the isotopic signature of moisture originating from Arctic
524 sources is generally marked by maxima in both $\delta^{18}\text{O}$ and d-excess. According to these conclusions,
525 seasonal changes in the moisture source could thus explain the opposite correlation observed in
526 winter and in summer in our dataset. Yet, the positive correlation observed during winter in our
527 dataset is largely driven by the extreme low d-excess values observed during the coldest and driest
528 periods, so this correlation should be taken with caution with respect to measurement artefacts.

529 It remains open which processes are most relevant for the observed changing relationship between
530 $\delta^{18}\text{O}$ and d-excess. Shifts in moisture origin, Rayleigh distillation along the transport pathway,
531 deposition/condensation under supersaturated conditions during transport, deposition of vapour
532 onto the snow surface, and snow sublimation into the atmosphere are all plausible mechanisms in
533 play for modulating the seasonal variability of our $\delta^{18}\text{O}$ and d-excess measurements. However, it can
534 be assumed that these processes exert varying degrees of influence during the different seasons and
535 POL positions with respect to the sea-ice margin, with kinetic fractionation associated to evaporation
536 and sublimation dominating in summer in proximity to the open ocean, and deposition/condensation
537 under supersaturated conditions prevailing in winter over the sea-ice.

538



539

540 *Figure 7: Scatterplots of water vapour $\delta^{18}\text{O}$ (top) and d-excess (bottom) versus local air temperature (left) and local specific*
 541 *humidity (right), here aggregated at 3 h resolution. The annual dataset (Oct 2019-Sept 2020) is displayed in grey, summer (JJA)*
 542 *values are coloured in light green and winter (DJF) values in teal. Values retrieved in humidity conditions lower than 0.4 g kg^{-1}*
 543 *are marked as triangles, else as circles. The linear regression line for the annual dataset is illustrated as a black dashed line; seasonal*
 544 *linear regressions in blue.*

545

546

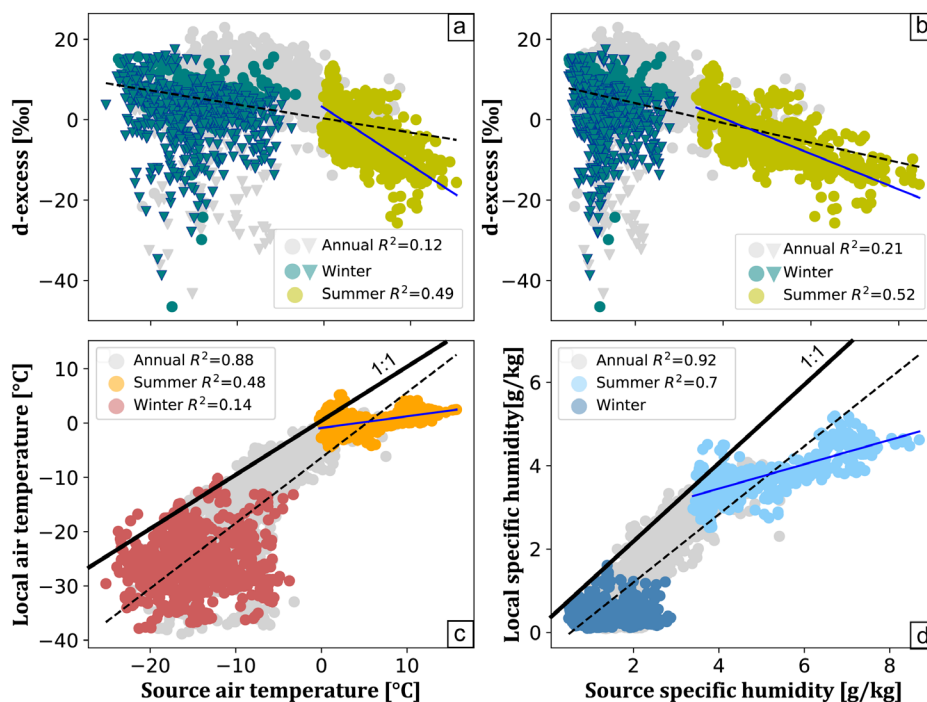
547 4.3 Linking measured d-excess changes to evaporative conditions at the moisture source

548

549 From the moisture source analyses (Sec. 3.3) we conclude that changes in moisture uptake regions
 550 are likely to modulate the sensitivity of the water vapour isotopes to both local and regional
 551 temperature. In summer, the highest evaporation rates occurred from the ice-free ocean surface and
 552 the largest contribution is identified near POL, suggesting proximal moisture uptake. In accordance,
 553 the results from the FLEXPART analysis reveal low residence time of the related air masses over sea-
 554 ice and land. Thus, changes in temperature and humidity conditions over the oceanic moisture
 555 uptake regions determine the changes in the isotopic signature of vapour at POL, without strong
 556 interference from air mass transformation during the advection. We conclude that air masses
 557 sampled during summer preserved the isotopic composition of vapour associated to primary
 558 evaporation from nearby ocean waters. During winter on the other hand, the moisture sources of the
 559 air masses were in general much more distant from POL. The backward trajectories reveal high
 560 residence times over ocean and sea-ice and, to a minor extent, over Siberia, for such transport
 561 pathways. The extended residency of air masses over sea-ice, along with the correlation of stable
 562 water isotopes to surface temperature in the ice-covered region, together suggest an influence of
 563 moisture exchange processes over the sea-ice area.

564 To further test this hypothesis, we examine the relationship between d-excess and the meteorological
 565 conditions in the source regions. We computed the weighted averages of T2m and Q2m from ERA5,
 566 based on the moisture uptake values retrieved from the trajectory-based moisture source diagnostic

567 (Sec. 3.3). To do so, a weight has been assigned to each uptake location according to its contribution
 568 to the total moisture uptake in a given time step, and a weighted average of the meteorological
 569 quantities was computed. We obtained time series of meteorological conditions at the total
 570 evaporative source, hereafter referred as T_{source} and Q_{source} , which we correlated with the local
 571 observations at POL (Figure 8). Panels a, b show the relationship of the d-excess observations and
 572 T_{source} and Q_{source} , respectively. Changes in d-excess correlate to source conditions in summer, but not
 573 in winter. During summer, the relationship with source temperature does not differ greatly from the
 574 one obtained with local temperature. The slope of d-excess and T_{source} is $-1.4\text{‰ }^{\circ}\text{C}^{-1}$, slightly lower
 575 than $-1.8\text{‰ }^{\circ}\text{C}^{-1}$ for T_{local} . However, for Q_{source} , the slope is $-4.4\text{‰ }(\text{g}/\text{kg})^{-1}$, half the one obtained for
 576 Q_{local} $-8.15\text{‰ }(\text{g}/\text{kg})^{-1}$. Hence, d-excess has a higher sensitivity to local humidity.
 577



578
 579
 580 *Figure 8: Upper panels: scatterplots of atmospheric water vapour d-excess and air temperature (a) and specific humidity (b)*
 581 *averaged over the moisture uptake regions. Lower panels: scatterplots of local and source air temperature (c) and specific*
 582 *humidity (d). The local meteorological data are obtained from the weather station operated onboard Polarstern, the source*
 583 *meteorological data are obtained from the ERA5 reanalyses from ECMWF. All datasets are aggregated at 3 h time resolution.*
 584 *Regression lines for the annual datasets are illustrated as a dashed black line while regression lines for the summer values are*
 585 *illustrated by the blue solid line.*

586 To investigate the covariance of local and source temperature and humidity conditions, we compared
 587 Q_{source} and T_{source} to Q_{local} and T_{local} (Figure 8c, d). In summer, when moisture uptake takes place all
 588 over the Arctic basin, including coastal regions, we observe a positive correlation between the local
 589 and source variables. However, the regression line deviates from the 1:1 line and the final slopes are
 590 0.21 and 0.30 for temperature and humidity, respectively. While T_{source} spans a variability range of
 591 $\sim 15^{\circ}\text{C}$, T_{local} remains relatively constrained around 0°C . The correlation between local and source
 592 temperature conditions over summer is only slightly lower than the correlation observed between
 593 water vapour d-excess and source temperatures. These findings suggest that the influence of source
 594 conditions alone accounts for only a minor portion of the variations in d-excess. However, the relative

595 changes in evaporative temperature and humidity persist throughout the distillation pathway of the
596 air masses.

597 In contrast, during winter, we find no correlation between local and source conditions (Fig. 8c, d), or
598 between measured d-excess and T_{source} or Q_{source} (Fig. 8a, b). These results support our hypothesis of
599 air mass transformation during advection to the Central Arctic in winter time. Similarly to the air
600 mass transformation dynamics described in Thurnherr et al. (2021), where warm sectors of
601 extratropical cyclones experience net moisture loss due to dew deposition over the relatively colder
602 ocean and due to the formation of clouds in ascending air parcels, we postulate that during winter,
603 moisture loss over the Arctic sea-ice, under kinetic conditions, overprints the isotopic signal
604 associated with evaporative source conditions. Given the small amount of moisture originating at the
605 evaporative site (Barents Sea) and the long transport distance to reach the sampling location, the
606 final isotopic composition of vapour reaching POL might reflect the integrated influence of moisture
607 exchange under supersaturated conditions, such as during ice-cloud formation or solid deposition
608 onto the sea-ice. This hypothesis gains support from (i) the spatial correlation analysis (Fig. 3), where
609 winter vapour isotopes mostly display correlation with the ambient conditions over sea-ice covered
610 regions; (ii) by the moisture uptake analyses (Fig. 4d), where the trajectories of the air masses span
611 hundreds of kilometres over sea-ice covered regions.

612

613 *4.3.1 Linkage to source SST and RH_{skin}*

614 During summer, we obtain a negative correlation of measured d-excess values with the sea surface
615 temperatures of the moisture uptake regions (slope $-1.2\text{‰ }^{\circ}\text{C}^{-1}$, $R^2 = 0.45$, Fig. S4a), but no correlation
616 is found with RH_{skin} (Fig. S4b). Anticorrelation between water vapour d-excess and RH_{sst} at source
617 was documented by Pfahl and Wernli (2008) in the Mediterranean basin, and was also observed in
618 the Atlantic and the Southern Ocean (Thurnherr et al. 2021, Bonne et al., 2019, Uemura et al., 2008).
619 This relationship describes the out of equilibrium fractionation during evaporation from the open
620 ocean (Craig and Gordon, 1965) and highlights the role of the relative humidity gradient within the
621 air column at the evaporation site. We do not have a conclusive explanation to reconcile our
622 observations to the previous datasets. The link between d-excess to evaporative source conditions
623 remains to be proven in the Central Arctic and our results suggests that this relationship may not be
624 easy to assess where moisture sources include extensive land and sea-ice covered regions.

625

626

627 *4.4 Inferences from the ECHAM6-wiso simulation results*

628

629 In the previous model version ECHAM5-wiso, systematically too high $\delta^{18}\text{O}$ values were found in the
630 Arctic region compared to near-surface vapour isotope measurements by Bonne et al. (2019). The
631 authors identified the sublimation of snow deposited on top of sea-ice as an important process
632 depleting the isotopic composition of near-surface vapour. They proposed a parameterisation of the
633 isotopic composition of the snow layer on sea-ice, which depends on the isotopic composition of the
634 snowfall. This new parameterisation, which was missing in ECHAM5-wiso and is now implemented
635 in ECHAM6-wiso (Cauquoin and Werner, 2021), might have contributed to the good match between
636 measured and modelled $\delta^{18}\text{O}$ changes in summer 2020, although it may also be responsible for an
637 over-correction as the values are now slightly too depleted (Figure 6). Despite the deviation from the
638 1:1-line, correlation values and slopes suggest that for Arctic summer conditions the ECHAM6-wiso
639 model successfully reproduces local evaporation processes and related isotope fractionation at the
640 location of POL.

641 Concerning d-excess, a prominent mismatch between modelled and observed values occurs in the
642 transition between winter and spring (Fig.2, Figure S5). In this period, the most negative d-excess
643 values (as low as -33.5‰) of the entire dataset are observed, whereas ECHAM6-wiso simulates
644 positive d-excess values, up to 20‰. This mismatch is associated to a synoptic condition,
645 characterized by the coldest and driest weeks of the entire sampling campaign, during which no
646 moisture uptake was identified and a maximum residence time over sea-ice was detected. We
647 hypothesize that during this time, the air masses underwent intense distillation under
648 supersaturated conditions along their transport, resulting in both low $\delta^{18}\text{O}$ and d-excess values.
649 Further, atmospheric stability (instability) is typically associated with a stratified (unstable) lower
650 atmosphere where the snow surface is warmer (colder) than the air above, leading to positive
651 (negative) latent heat flux in form of sublimation (deposition) between near-surface atmospheric
652 water vapour and surface snow. Insights about potential surface moisture exchange processes will
653 arise from the investigation of isotopic relationships between water vapour and the snow discrete
654 samples collected during MOSAiC (Mellat et al., 2022, Macfarlane et al., 2021). More detailed process-
655 based studies, with a focus on hoar formation and fog might also provide key insights into the
656 coupling between air masses and sea-ice. The description of the processes leading to negative d-
657 excess values is expected to remain partly speculative due to the uncertainties associated with our
658 negative d-excess measurements. For future campaigns, we strongly advocate for implementing
659 dedicated technical solutions (Leroy DosSantos, 2021) to increase instrumental accuracy at very low
660 humidity levels (<400 ppmv).

661 In addition to these specific explanations for the found model-data discrepancies, there are a few
662 more model deficits worth mentioning. The current ECHAM6-wiso model version has proven to
663 reproduce high-resolution temporal isotopic variations well (Cauquoin and Werner 2021), however
664 some interactions between the cryosphere and atmosphere could still be improved. E.g., no
665 fractionation during sublimation is considered in ECHAM6-wiso, despite recent studies observing
666 kinetic fractionation during snow post-depositional processes (Casado et al., 2018) and during
667 sublimation of snow to the atmosphere (Wahl et al., 2021, 2022). Furthermore, the isotopic
668 parameterisation of precipitation under supersaturation conditions is tuned to match the observed
669 Antarctic snow, without evidence that this relationship may be representative of the Arctic region
670 (Dütsch et al., 2019). Moreover, our ECHAM6-wiso simulation setup prescribes the sea-ice coverage
671 from ERA5 data which do not account for the presence of melt ponds and leads. The influence of such
672 small open water bodies on the isotope signal of water vapour is still subject to debate. Klein et al.
673 (2016) argued that sea-ice extent primarily acts on the distillation path depleting the air masses and
674 causing strong kinetic fractionation during evaporation from local sources such as leads and
675 polynyas. Whether these small-scale processes indeed can have a cumulative effect and an imprint
676 on the near-surface water vapour at the regional scale remains to be demonstrated. High-resolution
677 gridded datasets of lead fraction (Melsheimer & Spreen, 2019) and melt ponds (Webster et al., 2022)
678 might be used in future ECHAM6-wiso studies to prescribe the presence of liquid water on the sea-
679 ice. In addition, numerical modelling of isotope fractionation at the snow-air interphase will provide
680 a first-order understanding on the role of the cryosphere to impact the water vapour at the regional
681 and seasonal scale, especially in winter. Coupled simulations of AGCMs with a complex snowpack
682 model enabled for water isotopes fractionation (CROCUS, Touzeau et al., 2018) might also allow an
683 improved assessment of the contributions of such processes in the Arctic realm.

684
685

686 **5. Conclusions**

687
688 During the MOSAiC drifting campaign, we operated an autonomous water vapour isotope analyser
689 onboard the research vessel Polarstern (POL). In this study, we present the atmospheric water
690 vapour isotopes measurements, spanning an entire annual cycle from October 2019 to September
691 2020. We observed a seasonal cycle in water vapour $\delta^{18}\text{O}$, which mimics the seasonal changes in local
692 temperature and humidity. The isotopic composition of the summer moisture correlates with surface
693 temperature and humidity over the ocean sector and the margin of the sea-ice, while winter moisture
694 is associated to changes in near-surface conditions over the sea-ice. To investigate whether these
695 differences are a consequence of different moisture origin, we combine isotopic measurements with
696 a moisture source analysis, based on semi-Lagrangian back-trajectory simulations. During the
697 summer season, we observed significant moisture uptake in proximity to the sampling site, at the
698 margin of the retreating sea-ice. The environmental conditions at these evaporative sites correlate
699 with those at the location of POL, and with the water vapour d-excess signal. Thus, we infer that
700 during summer the water vapor isotopes retain valuable information about source temperature and
701 humidity. In contrast, winter moisture sampled during MOSAiC originated over the sea-ice-free
702 region of the Barents Sea. This is an important finding, in consideration that the Barents Sea has
703 undergone severe sea-ice loss in recent decades and may act as a progressively more prominent
704 source of winter moisture for the Arctic realm. However, we found no correlation between
705 evaporative source conditions and the d-excess signal measured in the water vapour onboard POL.
706 Results from an isotope-enabled ECHAM6-wiso simulation indicate that evaporative processes from
707 the open ocean and distillation along the transport (under isotopic equilibrium conditions) are not
708 sufficient to explain our observations. We suggest that non-equilibrium isotopic fractionation
709 processes during the transport over sea-ice, beyond what is currently included in the used ECHAM6-
710 wiso atmosphere model, are key to modulating the d-excess values in Arctic moisture in winter.
711 Considering the uncertainties in the parameterization of kinetic fractionation in supersaturated
712 conditions, we advocate for future sensitivity studies to assess the isotopic signature associated to
713 ice or mixed-phase clouds, as well as solid deposition on the snow surface under supersaturated
714 conditions.

715 This study delivers a baseline for understanding Arctic moisture origin and transport pathways in
716 the current warming climate. However, it also carries a high level of complexity due to the
717 spatiotemporal variability of the signal acquired along a drifting track and the uncertainties
718 associated with both the isotopic measurements and the moisture source diagnostics in extremely
719 cold and dry conditions. Yet, as the understanding of the Arctic water cycle and the ability to model
720 its future change is limited by the paucity of observations, our dataset of stable water isotope
721 observations can serve as a unique benchmark to test the sensitivity of climate models and their
722 parameterisation.

723
724

725 **Open Research**

726 The calibrated near-surface atmospheric water vapour isotopes measurements (Brunello et al.,
727 2022a, b,c,d,e) and the continuous meteorological surface measurements (Schmithüsen 2021a,
728 b,c,d,e) obtained during the MOSAiC campaign are published in the data repository PANGEA. This
729 study uses ERA5 hourly data at the surface (Hersbach et al., 2023), available at Copernicus Climate
730 Change Service, Climate Data Store. The ECHAM6-wiso simulation (Cauquoin and Werner, 2021) was
731 performed at the Alfred Wegener Institute supercomputing centre. The ECHAM model code is

732 available under a version of the MPI-M software license agreement. The code of the isotopic version
733 ECHAM6-wiso is available upon request on AWI's GitLab repository.

734

735

736 **Acknowledgements**

737 The authors declare no real or perceived financial conflicts of interests in regard of this work. The
738 data used in this manuscript were produced as part of the international Multidisciplinary drifting
739 Observatory for the Study of the Arctic Climate (MOSAiC) with the tag MOSAiC20192020. We thank
740 all those who contributed to MOSAiC and made this endeavour possible (Nixdorf et al. 2021). This
741 study was carried out as part of the project “Changes of water isotopes in Arctic Sea-ice, Ocean and
742 atMosphere” (CiASOM), which received support from the German Federal Ministry of Education and
743 Research (BMBF, award no. 03F0869A). The authors acknowledge the assistance of J.-L. Bonne, S.
744 Bagheri and M. Behrens for the design, set up and support regarding the custom-designed calibration
745 module. We thank J. Welker and B. Kopec for the helpful discussions about atmospheric transport
746 pathways across the Arctic region.

747

748

749 **References**

- 750 Aemisegger, F. (2018). On the link between the North Atlantic storm track and precipitation
751 deuterium excess in Reykjavik. *Atmospheric Science Letters*, 19(12). doi: 10.1002/asl.865
- 752 Bailey, H., Hubbard, A., Klein, E. S., Mustonen, K. R., Akers, P. D., Marttila, H., & Welker, J. M. (2021).
753 Arctic sea-ice loss fuels extreme European snowfall. *Nature Geoscience*, 14(5), 283-+.
754 doi:10.1038/s41561-021-00719-y
- 755 Bastrikov, V., Steen-Larsen, H. C., Masson-Delmotte, V., Gribanov, K., Cattani, O., Jouzel, J., &
756 Zakharov, V. (2014). Continuous measurements of atmospheric water vapour isotopes in
757 western Siberia (Kourovka). *Atmospheric Measurement Techniques*, 7(6), 1763-1776.
758 doi:10.5194/amt-7-1763-2014
- 759 Bengtsson, L., Hodges, K. I., Koumoutsaris, S., Zahn, M., & Keenlyside, N. (2011). The changing
760 atmospheric water cycle in Polar Regions in a warmer climate. *Tellus Series a-Dynamic
761 Meteorology and Oceanography*, 63(5), 907-920. doi:10.1111/j.1600-0870.2011.00534.x
- 762 Berkelhammer, M., Noone, D. C., Wong, T. E., Burns, S. P., Knowles, J. F., Kaushik, A., . . . Williams, M.
763 W. (2016). Convergent approaches to determine an ecosystem's transpiration fraction.
764 *Global Biogeochemical Cycles*, 30(6), 933-951. doi:10.1002/2016gb005392
- 765 Bintanja, R. (2018). The impact of Arctic warming on increased rainfall. *Scientific Reports*, 8.
766 doi:10.1038/s41598-018-34450-3
- 767 Bintanja, R., & Selten, F. M. (2014). Future increases in Arctic precipitation linked to local
768 evaporation and sea-ice retreat. *Nature*, 509(7501), 479-+. doi:10.1038/nature13259
- 769 Bolot, M., Legras, B., & Moyer, E. J. (2013). Modelling and interpreting the isotopic composition of
770 water vapour in convective updrafts. *Atmospheric Chemistry and Physics*, 13(16), 7903-
771 7935.
- 772 Bonne, J. L., Behrens, M., Meyer, H., Kipfstuhl, S., Rabe, B., Schönicke, L., . . . Werner, M. (2019).
773 Resolving the controls of water vapour isotopes in the Atlantic sector. *Nat Commun*, 10(1),
774 1632. doi:10.1038/s41467-019-09242-6
- 775 Bonne, J. L., Masson-Delmotte, V., Cattani, O., Delmotte, M., Risi, C., Sodemann, H., & Steen-Larsen, H.
776 C. (2014). The isotopic composition of water vapour and precipitation in Ivittuut, southern

777 Greenland. *Atmospheric Chemistry and Physics*, 14(9), 4419-4439. doi:10.5194/acp-14-
778 4419-2014

779 Bonne, J. L., Meyer, H., Behrens, M., Boike, J., Kipfstuhl, S., Rabe, B., . . . Werner, M. (2020). Moisture
780 origin as a driver of temporal variabilities of the water vapour isotopic composition in the
781 Lena River Delta, Siberia. *Atmospheric Chemistry and Physics*, 20(17), 10493-10511.
782 doi:10.5194/acp-20-10493-2020

783 Bonne, J. L., Steen-Larsen, H. C., Risi, C., Werner, M., Sodemann, H., Lacour, J. L., . . . Masson-Delmotte,
784 V. (2015). The summer 2012 Greenland heat wave: In situ and remote sensing observations
785 of water vapor isotopic composition during an atmospheric river event. *Journal of*
786 *Geophysical Research-Atmospheres*, 120(7), 2970-2989. doi:10.1002/2014jd022602

787 Breant, C., Dos Santos, C. L., Agosta, C., Casado, M., Fourre, E., Goursaud, S., . . . Landais, A. (2019).
788 Coastal water vapor isotopic composition driven by katabatic wind variability in summer at
789 Dumont d'Urville, coastal East Antarctica. *Earth and Planetary Science Letters*, 514, 37-47.
790 doi:10.1016/j.epsl.2019.03.004

791 Brunello, Camilla F; Werner, Martin; Meyer, Hanno; Mellat, Moein; Bonne, Jean-Louis (2022a):
792 Continuous near-surface atmospheric water vapour isotopic composition from Polarstern
793 cruise PS122-1 (MOSAIC). PANGAEA, <https://doi.org/10.1594/PANGAEA.951424>

794 Brunello, Camilla F; Werner, Martin; Meyer, Hanno; Mellat, Moein; Bonne, Jean-Louis (2022b):
795 Continuous near-surface atmospheric water vapour isotopic composition from Polarstern
796 cruise PS122-2 (MOSAIC). PANGAEA, <https://doi.org/10.1594/PANGAEA.951446>

797 Brunello, Camilla F; Werner, Martin; Meyer, Hanno; Mellat, Moein; Bonne, Jean-Louis (2022c):
798 Continuous near-surface atmospheric water vapour isotopic composition from Polarstern
799 cruise PS122-3 (MOSAIC). PANGAEA, <https://doi.org/10.1594/PANGAEA.951447>

800 Brunello, Camilla F; Werner, Martin; Meyer, Hanno; Mellat, Moein; Bonne, Jean-Louis (2022d):
801 Continuous near-surface atmospheric water vapour isotopic composition from Polarstern
802 cruise PS122-4 (MOSAIC). PANGAEA, <https://doi.org/10.1594/PANGAEA.951448>

803 Brunello, Camilla F; Werner, Martin; Meyer, Hanno; Mellat, Moein; Bonne, Jean-Louis (2022e):
804 Continuous near-surface atmospheric water vapour isotopic composition from Polarstern
805 cruise PS122-5 (MOSAIC). PANGAEA, <https://doi.org/10.1594/PANGAEA.951449>

806 Butzin, M., Werner, M., Masson-Delmotte, V., Risi, C., Frankenberg, C., Griбанov, K., . . . Zakharov, V. I.
807 (2014). Variations of oxygen-18 in West Siberian precipitation during the last 50 years.
808 *Atmospheric Chemistry and Physics*, 14(11), 5853-5869. doi:10.5194/acp-14-5853-2014

809 Casado, M., Landais, A., Picard, G., Münch, T., Laepple, T., Stenni, B., . . . Jouzel, J. (2018). Archival
810 processes of the water stable isotope signal in East Antarctic ice cores. *The Cryosphere*,
811 12(5), 1745-1766. doi:10.5194/tc-12-1745-2018

812 Casado, M., Landais, A., Picard, G., Arnaud, L., Dreossi, G., Stenni, B., & Prié, F. (2021). Water isotopic
813 signature of surface snow metamorphism in Antarctica. *Geophysical Research Letters*,
814 48(17), e2021GL093382

815 Cauquoin, A., & Werner, M. (2021). High-Resolution Nudged Isotope Modeling With ECHAM6-Wiso:
816 Impacts of Updated Model Physics and ERA5 Reanalysis Data. *Journal of Advances in*
817 *Modeling Earth Systems*, 13(11). doi:e2021MS00253210.1029/2021MS002532

818 Cauquoin, A., Werner, M., & Lohmann, G. (2019). Water isotopes - climate relationships for the mid-
819 Holocene and preindustrial period simulated with an isotope-enabled version of MPI-ESM.
820 *Climate of the Past*, 15(6), 1913-1937. doi:10.5194/cp-15-1913-2019

821 Cohen, J., Screen, J. A., Furtado, J. C., Barlow, M., Whittleston, D., Coumou, D., ... & Jones, J. (2014).
822 Recent Arctic amplification and extreme mid-latitude weather. *Nature geoscience*, 7(9),
823 627-637.

824 Cohen, J., Zhang, X., Francis, J., Jung, T., Kwok, R., Overland, J., . . . Yoon, J. (2020). Divergent
825 consensus on Arctic amplification influence on midlatitude severe winter weather. *Nature*
826 *Climate Change*, 10(1), 20-+. doi:10.1038/s41558-019-0662-y

827 Craig, H. (1961). Isotopic Variations in Meteoric Waters. *Science*, 133(3465), 1702-1703.
828 doi:10.1126/science.133.3465.1702

829 Craig, H., & Gordon, L. I. (1965). Deuterium and oxygen 18 variations in the ocean and the marine
830 atmosphere.

831 Dansgaard, W. (1964). Stable isotopes in precipitation. *tellus*, 16(4), 436-468.

832 Dutsch, M., Blossey, P. N., Steig, E. J., & Nusbaumer, J. M. (2019). Nonequilibrium Fractionation
833 During Ice Cloud Formation in iCAM5: Evaluating the Common Parameterization of
834 Supersaturation as a Linear Function of Temperature. *Journal of Advances in Modeling Earth*
835 *Systems*, 11(11), 3777-3793. doi:10.1029/2019ms001764

836 Dutsch, M., Pfahl, S., & Wernli, H. (2016). Drivers of delta H-2 variations in an idealized extratropical
837 cyclone. *Geophysical Research Letters*, 43(10), 5401-5408. doi:10.1002/2016gl068600

838 Ellehoj, M. D., Steen-Larsen, H. C., Johnsen, S. J., & Madsen, M. B. (2013). Ice-vapor equilibrium
839 fractionation factor of hydrogen and oxygen isotopes: experimental investigations and
840 implications for stable water isotope studies. *Rapid Commun Mass Spectrom*, 27(19), 2149-
841 2158. doi:10.1002/rcm.6668

842 Fremme, A. and Sodemann, H. (2019), The role of land and ocean evaporation on the variability of
843 precipitation in the Yangtze River valley, *Hydrol. Earth Syst. Sci.*, 23, 2525-2540, 2019
844 <https://doi.org/10.5194/hess-23-2525-2019>

845 Gat, J. R. (1996). Oxygen and hydrogen isotopes in the hydrologic cycle. *Annual Review of Earth and*
846 *Planetary Sciences*, 24, 225-262. doi:DOI 10.1146/annurev.earth.24.1.225

847 Graham, R. M., Hudson, S. R., & Maturilli, M. (2019). Improved Performance of ERA5 in Arctic
848 Gateway Relative to Four Global Atmospheric Reanalyses. *Geophysical Research Letters*,
849 46(11), 6138-6147. doi:10.1029/2019gl082781

850 Hersbach, H., Bell, B., Berrisford, P., Biavati, G., Horányi, A., Muñoz Sabater, J., Nicolas, J., Peubey, C.,
851 Radu, R., Rozum, I., Schepers, D., Simmons, A., Soci, C., Dee, D., Thépaut, J-N. (2023): ERA5
852 hourly data on single levels from 1940 to present. Copernicus Climate Change Service (C3S)
853 Climate Data Store (CDS), DOI: 10.24381/cds.adbb2d47

854 Hoffmann, G., Werner, M., & Heimann, M. (1998). Water isotope module of the ECHAM atmospheric
855 general circulation model: A study on timescales from days to several years (vol 103, pg
856 16871, 1998). *Journal of Geophysical Research-Atmospheres*, 103(D18), 23323-23323.
857 Retrieved from <Go to ISI>://WOS:000076302900024

858 Holland, M. M., & Bitz, C. M. (2003). Polar amplification of climate change in coupled models. *Climate*
859 *Dynamics*, 21(3-4), 221-232. doi:10.1007/s00382-003-0332-6

860 Hu, J., Yan, Y. Z., Yeung, L. Y., & Dee, S. G. (2022). Sublimation Origin of Negative Deuterium Excess
861 Observed in Snow and Ice Samples From McMurdo Dry Valleys and Allan Hills Blue Ice
862 Areas, East Antarctica. *Journal of Geophysical Research-Atmospheres*, 127(11).
863 doi:e2021JD03595010.1029/2021JD035950

864 Huang, J. B., Zhang, X. D., Zhang, Q. Y., Lin, Y. L., Hao, M. J., Luo, Y., . . . Zhang, J. S. (2017). Recently
865 amplified arctic warming has contributed to a continual global warming trend. *Nature*
866 *Climate Change*, 7(12), 875-+. doi:10.1038/s41558-017-0009-5

867 Hughes, A. G., Wahl, S., Jones, T. R., Zuhr, A., Horhold, M., White, J. W. C., & Steen-Larsen, H. C. (2021).
868 The role of sublimation as a driver of climate signals in the water isotope content of surface
869 snow: laboratory and field experimental results. *Cryosphere*, 15(10), 4949-4974.
870 doi:10.5194/tc-15-4949-2021

871 Jouzel, J., & Merlivat, L. (1984). Deuterium and oxygen 18 in precipitation: Modeling of the isotopic
872 effects during snow formation. *Journal of Geophysical Research: Atmospheres*, 89(D7),
873 11749-11757.

874 Klein, E. S., & Welker, J. M. (2016). Influence of sea ice on ocean water vapor isotopes and Greenland
875 ice core records. *Geophysical Research Letters*, 43(24), 12475-12483.
876 doi:10.1002/2016gl071748

877 Kopec, B. G., Feng, X., Posmentier, E. S., & Sonder, L. J. (2019). Seasonal Deuterium Excess Variations
878 of Precipitation at Summit, Greenland, and their Climatological Significance. *Journal of*
879 *Geophysical Research-Atmospheres*, 124(1), 72-91. doi:10.1029/2018jd028750

880 Kopec, B. G., Feng, X. H., Michel, F. A., & Posmentier, E. S. (2016). Influence of sea ice on Arctic
881 precipitation. *Proceedings of the National Academy of Sciences of the United States of*
882 *America*, 113(1), 46-51. doi:10.1073/pnas.1504633113

883 Kurita, N. (2011). Origin of Arctic water vapor during the ice-growth season. *Geophysical Research*
884 *Letters*, 38(2), n/a-n/a. doi:10.1029/2010gl046064

885 Lamb, K. D., Clouser, B. W., Bolot, M., Sarkozy, L., Ebert, V., Saathoff, H., ... & Moyer, E. J. (2017).
886 Laboratory measurements of HDO/H₂O isotopic fractionation during ice deposition in
887 simulated cirrus clouds. *Proceedings of the National Academy of Sciences*, 114(22), 5612-
888 5617.

889 Leroy-Dos Santos, C., Casado, M., Prie, F., Jossoud, O., Kerstel, E., Farradeche, M., . . . Landais, A.
890 (2021). A dedicated robust instrument for water vapor generation at low humidity for use
891 with a laser water isotope analyzer in cold and dry polar regions. *Atmospheric Measurement*
892 *Techniques*, 14(4), 2907-2918. doi:10.5194/amt-14-2907-2021

893 Leroy-Dos Santos, C., Masson-Delmotte, V., Casado, M., Fourré, E., Steen-Larsen, H. C., Maturilli, M., . .
894 . Landais, A. (2020). A 4.5 Year-Long Record of Svalbard Water Vapor Isotopic Composition
895 Documents Winter Air Mass Origin. *Journal of Geophysical Research: Atmospheres*, 125(23).
896 doi:10.1029/2020jd032681

897 Majoube, M. (1971). Fractionnement en oxygène 18 et en deutérium entre l'eau et sa vapeur.
898 *Journal de Chimie Physique*, 68, 1423-1436.

899 Macfarlane, Amy R; Schneebeli, Martin; Dadic, Ruzica; Wagner, David N; Arndt, Stefanie; Clemens-
900 Sewall, David; Hämmerle, Stefan; Hannula, Henna-Reetta; Jaggi, Matthias; Kolabutin,
901 Nikolai; Krampe, Daniela; Lehning, Michael; Matero, Ilkka; Nicolaus, Marcel; Oggier, Marc;
902 Pirazzini, Roberta; Polashenski, Chris; Raphael, Ian; Regnery, Julia; Shimanchuck, Egor;
903 Smith, Madison M; Tavri, Aikaterini (2021): Snowpit raw data collected during the MOSAiC
904 expedition. PANGAEA, <https://doi.org/10.1594/PANGAEA.935934>

905 Mellat, Moein; Meyer, Hanno; Brunello, Camilla F; Arndt, Stefanie; Macfarlane, Amy R; Schneebeli,
906 Martin; Hörhold, Maria; Werner, Martin; Weiner, Mikaela; Marent, Andreas (2022): Stable
907 water isotopes of snow during MOSAiC expedition. PANGAEA,
908 <https://doi.org/10.1594/PANGAEA.948511>

909 Melsheimer, Christian; Spreen, Gunnar (2019): AMSR2 ASI sea ice concentration data, Arctic,
910 version 5.4 (NetCDF) (July 2012 - December 2019). PANGAEA,
911 <https://doi.org/10.1594/PANGAEA.898399>

912 Merlivat, L. (1978). Molecular Diffusivities of (H₂O)-O-16, (H₂O)-O-18 in Gases. *Journal*
913 *of Chemical Physics*, 69(6), 2864-2871. doi:10.1063/1.436884

914 Merlivat, L., & Jouzel, J. (1979). Global Climatic Interpretation of the Deuterium-Oxygen-18
915 Relationship for Precipitation. *Journal of Geophysical Research-Oceans*, 84(Nc8), 5029-5033.
916 doi:DOI 10.1029/jc084ic08p05029

917 Pisso, I., Sollum, E., Grythe, H., Kristiansen, N. I., Cassiani, M., Eckhardt, S., Arnold, D., Morton, D.,
918 Thompson, R. L., Groot Zwaafink, C. D., Evangeliou, N., Sodemann, H., Haimberger, L.,
919 Henne, S., Brunner, D., Burkhardt, J. F., Fouilloux, A., Brioude, J., Philipp, A., Seibert, P., and
920 Stohl, A.: The Lagrangian particle dispersion model FLEXPART version 10.4, *Geosci. Model*
921 *Dev.*, 12, 4955–4997, <https://doi.org/10.5194/gmd-12-4955-2019>, 2019

922 Pfahl, S., & Wernli, H. (2008). Air parcel trajectory analysis of stable isotopes in water vapor in the
923 eastern Mediterranean. *Journal of Geophysical Research-Atmospheres*, 113(D20).
924 doi:D2010410.1029/2008jd009839

925 Polarstern: Alfred-Wegener-Institut Helmholtz-Zentrum für Polar- und Meeresforschung. (2017).
926 Polar Research and Supply Vessel POLARSTERN Operated by the Alfred-Wegener-Institute.
927 Journal of large-scale research facilities, 3, A119. <http://dx.doi.org/10.17815/jlsrf-3-163>.

928 Rinke, A., Cassano, J. J., Cassano, E. N., Jaiser, R., & Handorf, D. (2021). Meteorological conditions
929 during the MOSAiC expedition. *Elementa: Science of the Anthropocene*, 9(1).
930 doi:10.1525/elementa.2021.00023

931 Ritter, F., Steen-Larsen, H. C., Werner, M., Masson-Delmotte, V., Orsi, A., Behrens, M., . . . Kipfstuhl, S.
932 (2016). Isotopic exchange on the diurnal scale between near-surface snow and lower
933 atmospheric water vapor at Kohnen station, East Antarctica. *Cryosphere*, 10(4), 1647-1663.
934 doi:10.5194/tc-10-1647-2016

935 Rogers, R. R., & Yau, M. K. A short course in cloud physics. *Bull. Amer. Meteor. Soc*, 45, 619.

936 Samuels-Crow, K. E., Galewsky, J., Sharp, Z. D., & Dennis, K. J. (2014). Deuterium excess in
937 subtropical free troposphere water vapor: Continuous measurements from the Chajnantor
938 Plateau, northern Chile. *Geophysical Research Letters*, 41(23), 8652-8659.

939 Schmithüsen, Holger (2021a): Continuous meteorological surface measurement during
940 POLARSTERN cruise PS122/1. Alfred Wegener Institute, Helmholtz Centre for Polar and
941 Marine Research, Bremerhaven, PANGAEA, <https://doi.org/10.1594/PANGAEA.935221>

942 Schmithüsen, Holger (2021b): Continuous meteorological surface measurement during
943 POLARSTERN cruise PS122/2. Alfred Wegener Institute, Helmholtz Centre for Polar and
944 Marine Research, Bremerhaven, PANGAEA, <https://doi.org/10.1594/PANGAEA.935222>

945 Schmithüsen, Holger (2021c): Continuous meteorological surface measurement during
946 POLARSTERN cruise PS122/3. Alfred Wegener Institute, Helmholtz Centre for Polar and
947 Marine Research, Bremerhaven, PANGAEA, <https://doi.org/10.1594/PANGAEA.935223>

948 Schmithüsen, Holger (2021d): Continuous meteorological surface measurement during
949 POLARSTERN cruise PS122/4. Alfred Wegener Institute, Helmholtz Centre for Polar and
950 Marine Research, Bremerhaven, PANGAEA, <https://doi.org/10.1594/PANGAEA.935224>

951 Schmithüsen, Holger (2021e): Continuous meteorological surface measurement during
952 POLARSTERN cruise PS122/5. Alfred Wegener Institute, Helmholtz Centre for Polar and
953 Marine Research, Bremerhaven, PANGAEA, <https://doi.org/10.1594/PANGAEA.935225>

954 Serreze, M. C., & Barry, R. G. (2011). Processes and impacts of Arctic amplification: A research
955 synthesis. *Global and Planetary Change*, 77(1-2), 85-96.
956 doi:10.1016/j.gloplacha.2011.03.004

957 Shupe, M. D., Rex, M., Blomquist, B., Persson, P. O. G., Schmale, J., Uttal, T., . . . Yue, F. G. (2022).
958 Overview of the MOSAiC expedition-Atmosphere INTRODUCTION. *Elementa-Science of the*
959 *Anthropocene*, 10(1). doi:110.1525/elementa.2021.00060

- 960 Sodemann, H., Schwierz, C., & Wernli, H. (2008). Interannual variability of Greenland winter
961 precipitation sources: Lagrangian moisture diagnostic and North Atlantic Oscillation
962 influence. *Journal of Geophysical Research: Atmospheres*, 113(D3).
- 963 Sodemann, H., and A. Stohl (2009), Asymmetries in the moisture origin of Antarctic precipitation,
964 *Geophys. Res. Lett.*, 36, L22803, doi:10.1029/2009GL040242.
- 965 Steen-Larsen, H. C., Johnsen, S. J., Masson-Delmotte, V., Stenni, B., Risi, C., Sodemann, H., . . . White, J.
966 W. C. (2013). Continuous monitoring of summer surface water vapor isotopic composition
967 above the Greenland Ice Sheet. *Atmospheric Chemistry and Physics*, 13(9), 4815-4828.
968 doi:10.5194/acp-13-4815-2013
- 969 Steen-Larsen, H. C., Sveinbjornsdottir, A. E., Jonsson, T., Ritter, F., Bonne, J. L., Masson-Delmotte, V., . .
970 . Vinther, B. M. (2015). Moisture sources and synoptic to seasonal variability of North
971 Atlantic water vapor isotopic composition. *Journal of Geophysical Research-Atmospheres*,
972 120(12), 5757-5774. doi:10.1002/2015jd023234
- 973 Stevens, B., Giorgetta, M., Esch, M., Mauritsen, T., Crueger, T., Rast, S., . . . Roeckner, E. (2013).
974 Atmospheric component of the MPI-M Earth System Model: ECHAM6. *Journal of Advances in*
975 *Modeling Earth Systems*, 5(2), 146-172. doi:10.1002/jame.20015
- 976 Stohl, A., Forster, C., Frank, A., Seibert, P., & Wotawa, G. (2005). Technical note: The Lagrangian
977 particle dispersion model FLEXPART version 6.2. *Atmospheric Chemistry and Physics*, 5,
978 2461-2474. doi:DOI 10.5194/acp-5-2461-2005
- 979 Thurnherr, I., Kozachek, A., Graf, P., Weng, Y., Bolshiyarov, D., Landwehr, S., . . . Aemisegger, F.
980 (2020). Meridional and vertical variations of the water vapour isotopic composition in the
981 marine boundary layer over the Atlantic and Southern Ocean. *Atmospheric Chemistry and*
982 *Physics*, 20(9), 5811-5835. doi:10.5194/acp-20-5811-2020
- 983 Thurnherr, I., Hartmuth, K., Jansing, L., Gehring, J., Boettcher, M., Gorodetskaya, I., ... & Aemisegger,
984 F. (2021). The role of air-sea fluxes for the water vapour isotope signals in the cold and
985 warm sectors of extratropical cyclones over the Southern Ocean. *Weather and Climate*
986 *Dynamics*, 2(2), 331-357.
- 987 Touzeau, A., Landais, A., Morin, S., Arnaud, L., & Picard, G. (2018). Numerical experiments on vapor
988 diffusion in polar snow and firn and its impact on isotopes using the multi-layer energy
989 balance model Crocus in SURFEX v8.0. *Geoscientific Model Development*, 11(6), 2393-2418.
990 doi:10.5194/gmd-11-2393-2018
- 991 Uemura, R., Matsui, Y., Yoshimura, K., Motoyama, H., & Yoshida, N. (2008). Evidence of deuterium
992 excess in water vapor as an indicator of ocean surface conditions. *Journal of Geophysical*
993 *Research-Atmospheres*, 113(D19). doi:D19114 10.1029/2008jd010209
- 994 Urey, H. C. (1947). The thermodynamic properties of isotopic substances. *Journal of the Chemical*
995 *Society (Resumed)*, 562-581. doi: 10.1039/JR9470000562
- 996 Vihma, T., Screen, J., Tjernstrom, M., Newton, B., Zhang, X. D., Popova, V., . . . Prowse, T. (2016). The
997 atmospheric role in the Arctic water cycle: A review on processes, past and future changes,
998 and their impacts. *Journal of Geophysical Research-Biogeosciences*, 121(3), 586-620.
999 doi:10.1002/2015jg003132
- 1000 Wahl, S., Steen-Larsen, H. C., Reuder, J., & Horhold, M. (2021). Quantifying the Stable Water
1001 Isotopologue Exchange Between the Snow Surface and Lower Atmosphere by Direct Flux
1002 Measurements. *Journal of Geophysical Research-Atmospheres*, 126(13). doi:e2020JD034400
1003 10.1029/2020JD034400
- 1004 Wang, C. X., Graham, R. M., Wang, K. G., Gerland, S., & Granskog, M. A. (2019). Comparison of ERA5
1005 and ERA-Interim near-surface air temperature, snowfall and precipitation over Arctic sea

1006 ice: effects on sea ice thermodynamics and evolution. *Cryosphere*, 13(6), 1661-1679.
1007 doi:10.5194/tc-13-1661-2019

1008 Werner, M., Langebroek, P. M., Carlsen, T., Herold, M., & Lohmann, G. (2011). Stable water isotopes
1009 in the ECHAM5 general circulation model: Toward high-resolution isotope modeling on a
1010 global scale. *Journal of Geophysical Research-Atmospheres*, 116.
1011 doi:D1510910.1029/2011jd015681

1012 Ye, K. H., & Messori, G. (2021). Inter-model spread in the wintertime Arctic amplification in the
1013 CMIP6 models and the important role of internal climate variability. *Global and Planetary
1014 Change*, 204. doi:10354310.1016/j.gloplacha.2021.103543

1015 Zahn, M., Akperov, M., Rinke, A., Feser, F., & Mokhov, I. I. (2018). Trends of Cyclone Characteristics
1016 in the Arctic and Their Patterns From Different Reanalysis Data. *Journal of Geophysical
1017 Research-Atmospheres*, 123(5), 2737-2751. doi:10.1002/2017jd027439

1018 Zhang, X. D., He, J. X., Zhang, J., Polyakov, I., Gerdes, R., Inoue, J., & Wu, P. L. (2013). Enhanced
1019 poleward moisture transport and amplified northern high-latitude wetting trend. *Nature
1020 Climate Change*, 3(1), 47-51. doi:10.1038/Nclimate1631

1021 Webster MA, Holland M, Wright NC, Hendricks S, Hutter N, et al. (2022). Spatiotemporal evolution
1022 of melt ponds on Arctic sea ice: MOSAiC observations and model results. *Elem Sci Anth*
1023 10(1): 000072.